PNAS RESEARCH ARTICLE | BIOCHEMISTRY OPEN ACCESS

The function of Mak16 in ribosome biogenesis depends on its [4Fe-4S] cluster

Nadine Duppe[a,1], Lukas Knauer[a,b], Marc Hagebölling[a,2], Lena Langner[a,3], Martin Stümpfig[c], Volker Schünemann[b], Antonio J. Pierik[a,4], and Daili J. Netz[a,4]

Affiliations are included on p. 10.

Edited by Markus W. Ribbe, University of California Irvine, Irvine, CA; received June 8, 2025; accepted October 12, 2025 by Editorial Board Member Marcetta Y. Darensbourg

Mak16 and its interacting partner Rpf1 play a critical role at an early step in the maturation of the ribosomal 60S subunit of eukaryotes, as revealed by cryoelectron microscopy structures. While these studies suggested no metal participation or the presence of a Zn^{2+} ion in Mak16, we identify a previously unexplored iron–sulfur (Fe/S) cluster in yeast Mak16 through both in vivo and in vitro methods. We demonstrate a functional link between mitochondrial and cytosolic Fe/S protein biogenesis and ribosome assembly, highlighting an overlooked aspect of 60S ribosomal biogenesis. Characterization of human and yeast Mak16 revealed a redox-active $[4Fe\text{-}4S]^{2+/1+}$ cluster with a midpoint potential below –500 mV. Oxidative stress destabilizes Mak16 and disrupts its interaction with Rpf1 in vivo, while in vitro H_2O_2 causes $[3Fe\text{-}4S]^{1+}$ cluster formation. Our findings also reveal that upon binding to rRNA expansion segment 7 the redox properties of the nearby Fe/S cluster largely remain unchanged. However, disruption of Fe/S cluster coordination destabilized Mak16, impaired the Mak16–Rpf1 complex formation and decreased the 25S rRNA level. The critical role of Fe/S proteins in eukaryotic DNA replication and repair, mitoribosomal function, and maturation has now been extended to nuclear ribosomal assembly. Relying on a vulnerable cofactor comes at a cost, as cluster loss can severely disrupt essential cellular processes. The inherent biosynthetic complexity and instability of the Fe/S cluster of Mak16 allows it to function as sensor for redox imbalance, creating the possibility to regulate cellular homeostasis under stress.

iron–sulfur | metallocofactor | ribosome biogenesis

Significance

This study identifies an iron–sulfur (Fe/S) cluster in the 60S ribosomal assembly factor Mak16 as essential for maintaining complex stability with its interacting partner Rpf1, which is crucial for the maturation of 25S ribosomal RNA (rRNA) during nuclear ribosome biogenesis. The [4Fe-4S] cluster of Mak16 displays redox properties typical of low-potential centers and is highly labile in the presence of oxygen and oxidative stress-inducing agents. Together, these features suggest that the Fe/S cluster of Mak16 plays a structural and potentially regulatory role in ribosome assembly. Our findings uncover an unappreciated requirement for an Fe/S cofactor in a key process in eukaryotic cells and expand the importance of Fe/S protein biosynthesis.

Iron–sulfur (Fe/S) clusters are ancient and essential metal cofactors, found in more than 100 eukaryotic proteins which fulfill critical functions in hallmark processes such as photosynthesis, citric acid cycle, and respiration (1). In addition to their established roles in electron transport, enzymatic catalysis, and gene regulation, Fe/S-containing proteins are pivotal in maintaining genomic stability by participating in DNA replication and repair, where they are critical cofactors of DNA polymerases, primase, helicases, and glycosylases (2). Fe/S proteins also play critical roles in transcription [RNA polymerase III (3) and transcription factor IIH (4)]. In the cytoplasm of yeast and humans the Rli1 protein utilizes its two [4Fe-4S] clusters to functionally support key stages of ribosome recycling (5), ensuring seamless transitions between initiation and elongation (6). Structural proteins of the human 28S and 39S mitochondrial ribosomal subunits harbor two and one [2Fe-2S] clusters, respectively, which enhance stability and support translational fidelity (7, 8). Moreover, the assembly of the small mitoribosomal subunit requires the [4Fe-4S] protein METTL17 (9).

In yeast, the assembly of the 40S and 60S ribosomal subunits begins in the nucleolus with the transcription of 35S rRNA, which contains the 18S, 5.8S, and 25S rRNAs. This process is guided by more than 100 accessory ribosomal proteins, that coordinate spatiotemporal events in ribosome maturation (10–12). The complexity of this biological process is enhanced by the involvement of metal ions, necessary for RNA folding, chemical modification, stability, and precise assembly (13). Mg^{2+} ions, which bind both to ribonucleotides and proteins, are extensively distributed in ribosomes. In contrast, transition metals such as Zn^{2+} are only coordinated by proteins (14). In recent years, several cryoelectron microscopy (cryo-EM) structures depicting distinct ribosomal precursors of the small and large subunits at various stages have contributed to the understanding of ribosome maturation (15–18). At an early stage, a key cotranscriptional assembly checkpoint is established by the binding of the Noc1-Noc2 assembly factors to Rrp5 (19). This checkpoint occurs just before 35S

Author contributions: A.J.P. and D.J.N. designed research; N.D., L.K., M.H., L.L., M.S., A.J.P., and D.J.N. performed research; N.D., L.K., V.S., A.J.P., and D.J.N. analyzed data; and N.D., A.J.P., and D.J.N. wrote the paper.

The authors declare no competing interest.

This article is a PNAS Direct Submission. M.W.R. is a guest editor invited by the Editorial Board.

Copyright © 2025 the Author(s). Published by PNAS. This open access article is distributed under Creative Commons Attribution License 4.0 (CC BY).

[1]Present address: BioNTech Innovative Manufacturing Services, Idar-Oberstein 55743, Germany.

[2]Present address: Dezernat 53 Immissionsschutz und anlagenbezogener Umweltschutz der Bezirksregierung, Münster 48147, Germany.

[3]Present address: Produktionsplanung, Mineralölraffinerie Oberrhein, Karlsruhe 76187, Germany.

[4]To whom correspondence may be addressed. Email: pierik@rptu.de or dnetz@rptu.de.

This article contains supporting information online at https://www.pnas.org/lookup/suppl/doi:10.1073/pnas.2513844122/-/DCSupplemental.

Published November 13, 2025.

Downloaded from https://www.pnas.org by Universitaetsbibliothek der RPTU Kaiserslautern-Landau on January 6, 2026 from IP address 131.246.60.80.

rRNA cleavage within the internal transcribed spacer 1, leading to the separation of the small and large ribosomal subunits. This event triggers the recruitment of a module consisting of Mak16, its partner protein Rpf1, the β-propeller protein Nsa1, and the α-helical protein Rrp1, which spatially constrains domains I and II of the 25S rRNA precursor (19).

Mak16 captured our attention due to the coimmunoprecipitation of the human homologue (MAK16) with the MMS19, CIA2B, and CIAO1 proteins, which form the Cytosolic Iron–sulfur protein Assembly (CIA) targeting complex responsible for the final step of Fe/S cluster insertion into apo-proteins (20, 21). In its N-terminal domain (NTD), Mak16 features a highly conserved cysteine motif capable of binding a Zn^{2+} ion or an Fe/S cluster. At a first glance, the hypothesis that Mak16 could be an Fe/S protein appeared incorrect, as in most cryo-EM structures Mak16 was either devoid of a metal ion, or Zn^{2+} binding was proposed (16–18). The resolution in cryo-EM structures poses challenges for precise metal ion positioning and identification due to the near-identical coordination environment for both Zn^{2+} and an Fe/S cluster. In this study, we performed a comprehensive analysis of the biophysical properties of recombinant yeast and human Mak16. We further interrogated in vivo Fe/S cluster assembly on Mak16 and explored the cellular consequences of defective assembly for Mak16 function in yeast. Our findings clarify the central question of metal occupancy in Mak16 and represent an important step toward understanding of the physiological significance of the Fe/S cluster of Mak16 in the context of 60S ribosome maturation.

Results

Mak16 from Different Eukaryotes Binds a Bona Fide Fe/S Cluster. The most effective approach to identify iron or Fe/S association with a eukaryotic protein is to analyze the full-length protein in its native organism (22). To this end, N-terminally HA-tagged yeast Mak16 was expressed from a single-copy plasmid under control of the *MET25* promoter in wild-type (W303) yeast cells. Radioactive ^{55}Fe was incorporated into cells, and its specific association with Mak16 was demonstrated through anti-HA immunoprecipitation. The analysis detected substantial ^{55}Fe binding to Mak16 at a level of 19 to 25 pmol/g of cells (Fig. 1*A*). Due to the approximately 20% efficiency of cell lysis, losses of 3xHA-Mak16 and its [4Fe–4S] cluster during immunoprecipitation, and residual Fe present even in Fe-free medium, the measured ^{55}Fe content cannot be directly converted into cluster occupancy per molecule. Nevertheless, the in vivo ^{55}Fe levels of Mak16 are consistent with those observed for other well-characterized yeast Fe/S proteins such as Pol3, Leu1, Rli1, Cfd1, Nbp35, Ntg2, and Nar1 [3 to 35 pmol/g (22, 23)] when expressed as full-length proteins in their native environments. Furthermore, as previously demonstrated (23), inadvertent ^{55}Fe incorporation into cysteine-rich proteins, including those with multiple zinc fingers, does not take place under these conditions.

To determine whether the ^{55}Fe originated from mononuclear, dinuclear, or Fe/S iron ions, we examined the dependence of ^{55}Fe-association with Mak16 on key Fe/S protein biogenesis factors. These included Nfs1, required for the assembly of all Fe/S

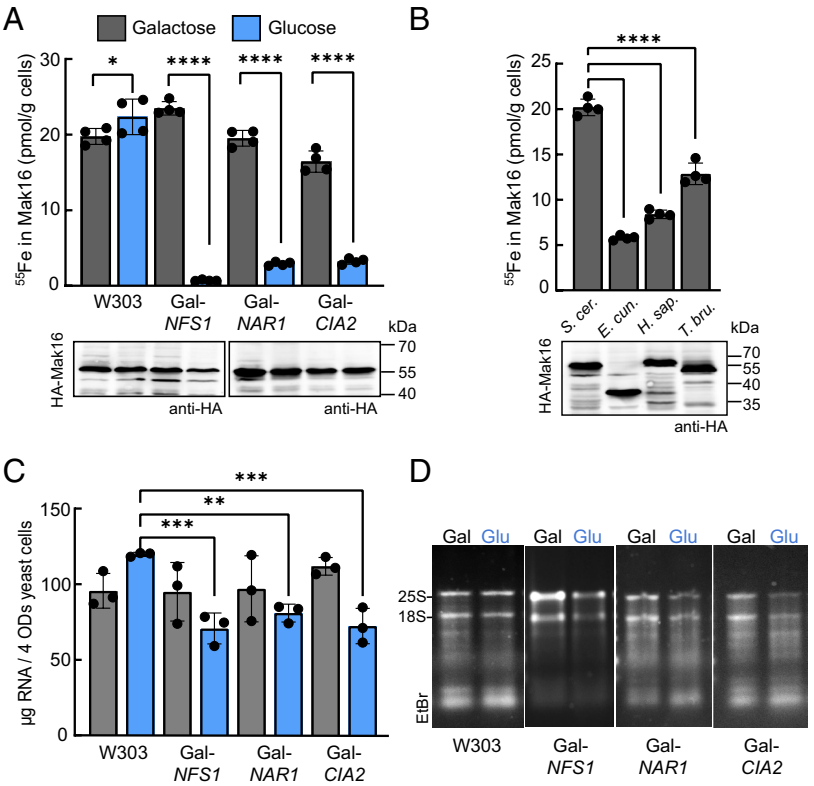


Fig. 1. Assembly of Fe/S clusters on Mak16 and efficient rRNA synthesis relies on the ISC and CIA machinery pathways. (*A*) Incorporation of ^{55}Fe in Mak16 in yeast strains expressing or depleted for ISC- or CIA-factors. The 416*MET25*-HA-Mak16 plasmid was transformed into W303, Gal-*NFS1*, Gal-*NAR1*, and Gal-*CIA2* yeast cells, grown in iron-poor SC medium supplemented with galactose or glucose and $^{55}FeCl_3$. HA-Mak16 was immunoprecipitated with anti-HA beads from cell extracts. Data are mean value ± SEM (n = 4). Significance of differences between groups, as indicated by crossbars, were determined using multiple comparisons one-way ANOVA with Šidák correction (*P < 0.05, ****P < 0.0001). (*B*) ^{55}Fe incorporation in Mak16 homologues expressed in W303 yeast cells in glucose containing SC medium as in (*A*). Abbreviations: *S. cer.*, *S. cerevisiae; H. sap.*, *Homo sapiens*; *E. cun.*, *Encephalitozoon cuniculi*; *T. bru.*, *Trypanosoma brucei*. ****P < 0.0001. (*C*) Total RNA isolated from W303 and yeast strains expressing or depleted for ISC- or CIA-factors. Yeast cells were cultured for 24 h in SC medium containing either galactose or glucose. Total RNA was then extracted from cells after two doubling times. n = 3, ***P < 0.001, **P < 0.01. (*D*) From the same samples used in (*C*) the RNA was separated by agarose gel electrophoresis and detected by GelRed staining.

Downloaded from https://www.pnas.org by Universitaetsbibliothek der RPTU Kaiserslautern-Landau on January 6, 2026 from IP address 131.246.60.80.

proteins, and the CIA components Nar1 and Cia2, involved in cytosolic and nuclear Fe/S protein maturation (24). For this purpose, galactose-regulatable strains were grown under permissive and repressive conditions (in galactose and glucose containing media, respectively, Fig. 1*A* and *SI Appendix*, Fig. S1). Upon efficient depletion of Nfs1, Nar1, or Cia2 proteins to undetectable levels on western blot (*SI Appendix*, Fig. S1 *C–E*), sufficient to cause biosynthetic phenotypes (22, 25, 26), ^{55}Fe incorporation into Mak16 was significantly impaired. This defect is consistent with the interconnected roles of the mitochondrial ISC and CIA pathways, establishing Mak16 as a bona fide Fe/S protein in vivo.

We then questioned whether Mak16 from phylogenetically distant homologues (*SI Appendix*, Fig. S2*A*), including human Mak16, also bind an Fe/S cluster upon expression in yeast cells. Significantly lower quantities of ^{55}Fe compared to yeast Mak16 were found in association with Mak16 homologs from humans, the microsporidial parasite *Encephalitozoon cuniculi*, and the kinetoplastic parasite *Trypanosoma brucei* (Fig. 1*B*, 6 to 13 pmol ^{55}Fe/g). These differences do not arise from variations in expression levels (Fig. 1 *B*, *Bottom* and *SI Appendix*, Fig. S2*B*), but may result from a diminished stability of the Fe/S cluster of Mak16 from these organisms, or the more effective Fe/S incorporation into yeast Mak16 by its own machinery in comparison with Fe/S incorporation into Mak16 from other organisms. Interestingly, Mak16 proteins (39 to 42 kDa) exhibit unusually low electrophoretic mobility on sodium dodecyl sulfate polyacrylamide gel electrophoresis (SDS-PAGE), probably due their acidic nature (pI ~ 4.9), except for Mak16 from *E. cuniculi* (33 kDa, pI = 8.7), which lacks the acidic C-terminal domain (Fig. 1*B*). To test whether these homologues, including human Mak16 (49% amino acid identity), could functionally substitute for yeast Mak16, a Gal-*MAK16* yeast strain was generated. In this galactose-regulatable strain, the endogenous *MAK16* promoter was replaced with the *GALL* promoter. Under permissive conditions (galactose-containing medium), cells transformed with plasmids expressing Mak16 homologues from different organisms, driven by either the native *MAK16* or the *MET25* promoter, showed no obvious growth differences (*SI Appendix*, Fig. S2*C*). Strikingly, upon depletion of endogenous yeast Mak16 in glucose-containing medium, only the ectopically expressed yeast Mak16 was able to rescue growth. None of the three Fe/S cluster-binding homologues, including human Mak16, restored viability, underscoring the species-specific functional integration of Mak16 in ribosome biogenesis (*SI Appendix*, Fig. S2*C*). Since yeast Mak16 functions in concert with Rpf1 and other ribosomal maturation factors (16), the inability of Mak16 homologues to rescue the loss of endogenous Mak16 may stem from a failure to engage these species-specific interaction partners. In summary, while the presence of an Fe/S cluster is a conserved feature of Mak16 proteins across phylogenetically diverse organisms, their functional integration into ribosome biogenesis appears to depend on precise molecular interactions with coevolved assembly factors.

To further assess whether impaired Fe/S cluster assembly into yeast Mak16 affects rRNA synthesis, total RNA was isolated from exponentially growing yeast cells. RNA levels were compared in glucose-grown cells following depletion of selected ISC and CIA components, specifically Nfs1, Cia2, and Nar1 (Fig. 1*C*). Both Nfs1 and Cia2 depletion resulted in strong decrease of total RNA levels, while the effect of Nar1 depletion, possibly due to a slightly slower onset, was less pronounced. Under permissive conditions (galactose), where Fe/S biogenesis remains active, total RNA was largely composed of rRNA [~80% (27)], with prominent 25S and 18S bands visible on denaturing gels (Fig. 1*D* and *SI Appendix*, Fig. S3). In glucose medium upon depletion of these Fe/S assembly factors, both 25S and 18S rRNA signals were diminished, with the 25S rRNA most strongly affected, despite equal total RNA loading. These results indicate that disruption of Fe/S cluster biogenesis impairs Mak16 function in ribosome biogenesis and reduces rRNA synthesis efficiency.

Human and Yeast Mak16 Proteins Contain a [4Fe-4S]$^{2+/1+}$ Cluster. To investigate the Fe/S cluster type and its biophysical properties, we expressed N-terminally hexahistidine tagged human and yeast Mak16 in *Escherichia coli*. Human Mak16 could be affinity purified under anaerobic conditions in absence of its interaction partners (*SI Appendix*, Fig. S4*A*). Ultraviolet-Visible (UV-Vis) spectroscopy of the beige protein showed a well-defined shoulder with a maximum at 400 nm (Fig. 2*A*), which was partially bleached upon dithionite reduction. The absence of characteristic UV-Vis absorption peaks at 330, 450, and 550 nm strongly suggests that human Mak16 does not harbor a [2Fe-2S] cluster, as reflected by its broad, featureless spectrum. The iron and acid-labile sulfide contents (2.6 ± 0.4 and 2.7 ± 1.2, respectively), together with an experimental extinction coefficient at 400 nm ($\varepsilon_{400\ nm}$ ~ 8.5 $mM^{-1}cm^{-1}$), indicate that purified human Mak16 contains either a nearly fully occupied $[3Fe\text{-}4S]^{1+}$ ($\varepsilon_{400\ nm}$ ~ 9.8 $mM^{-1}cm^{-1}$ per 3Fe), or a partially occupied $[4Fe\text{-}4S]^{2+}$ cluster ($\varepsilon_{400\ nm}$ ~ 13 $mM^{-1}cm^{-1}$ per 4Fe). The Mössbauer spectrum of human Mak16 isolated from ^{57}Fe-grown *E. coli* cells could be simulated with two equal intensity quadrupole doublets with almost identical isomer shifts (δ_1 = 0.42 and δ_2 = 0.44 mm/s) and slightly differing quadrupole splitting (ΔE_{Q1} = 0.99 and ΔE_{Q2} = 1.31 mm/s, Fig. 2*B* and *SI Appendix*, Table S1). These Mössbauer parameters differ from those of $[2Fe\text{-}2S]^{2+}$ and $[3Fe\text{-}4S]^{1+/0}$ clusters (28), but closely match the valence delocalized Fe^{2+}-Fe^{3+} pairs (2× $Fe^{2.5+}$) of all cysteine-coordinated protein-bound $[4Fe\text{-}4S]^{2+}$ clusters (Fig. 2*C* and *SI Appendix*, Table S2). The lack of a signal at g = 2.02 in the electron paramagnetic resonance (EPR) spectrum of ferricyanide oxidized human Mak16 corroborated the absence of $[3Fe\text{-}4S]^{0/1+}$. In agreement with the observed bleaching of the UV-Vis spectrum, dithionite reduction generated a prominent axial EPR signal with g_z = 2.00 and g_{yx} = 1.91 for the $[4Fe\text{-}4S]^{1+}$ cluster (Fig. 2*D*, EPR simulation parameters *SI Appendix*, Table S3). Dithionite treatment reduced approximately 75% of the [4Fe-4S] cluster, as evidenced by changes in the Mössbauer spectrum. Specifically, the isomer shifts of both quadrupole doublets increased upon reduction, reflecting changes in the electronic environment of the iron centers. Notably, the diferrous pair exhibited a larger increase in isomer shift compared to the other doublet, which remained intermediate between the values for mixed-valence $Fe^{2.5+}$ and diferrous Fe^{2+} pairs found in biological $[4Fe\text{-}4S]^{1+}$ clusters (Fig. 2*C* and *SI Appendix*, Table S4). Taken together, these findings show that human Mak16 contains a single cluster, with stable $[4Fe\text{-}4S]^{1+}$ and $[4Fe\text{-}4S]^{2+}$ oxidation states.

In contrast to human Mak16, yeast Mak16 proved difficult to purify to homogeneity (*SI Appendix*, Fig. S4*B*) and exhibited an unstable Fe/S cluster, with less than one iron per monomer *SI Appendix*, Fig. S4*C*). However, coexpression with its Brix-domain partner protein, yeast Rpf1, significantly enhanced the protein homogeneity (*SI Appendix*, Fig. S4*D*). Western blot analysis and Coomassie-stained SDS-PAGE showed a slow-migration His-Mak16 band (~50 kDa, despite a calculated mass of 37.3 kDa) alongside a distinct ~35 kDa band corresponding to Rpf1 (*SI Appendix*, Fig. S4*E*). Truncating the two N-terminal helices of Rpf1 (Rpf1-Δ58, *SI Appendix*, Fig. S5) further improved the homogeneity of the complex, resulting in a content of 3.9 ± 1.3 iron and 3.4 ± 0.8 sulfide per heterodimer. UV-visible (ε_{400nm} ~15 $mM^{-1}cm^{-1}$), and Mössbauer spectroscopy equally demonstrated the presence of a $[4Fe\text{-}4S]^{2+}$ cluster in the yeast Mak16/Rpf1-Δ58 complex (Fig. 2 *E* and *F*). Notably,

Downloaded from https://www.pnas.org by Universitaetsbibliothek der RPTU Kaiserslautern-Landau on January 6, 2026 from IP address 131.246.60.80.

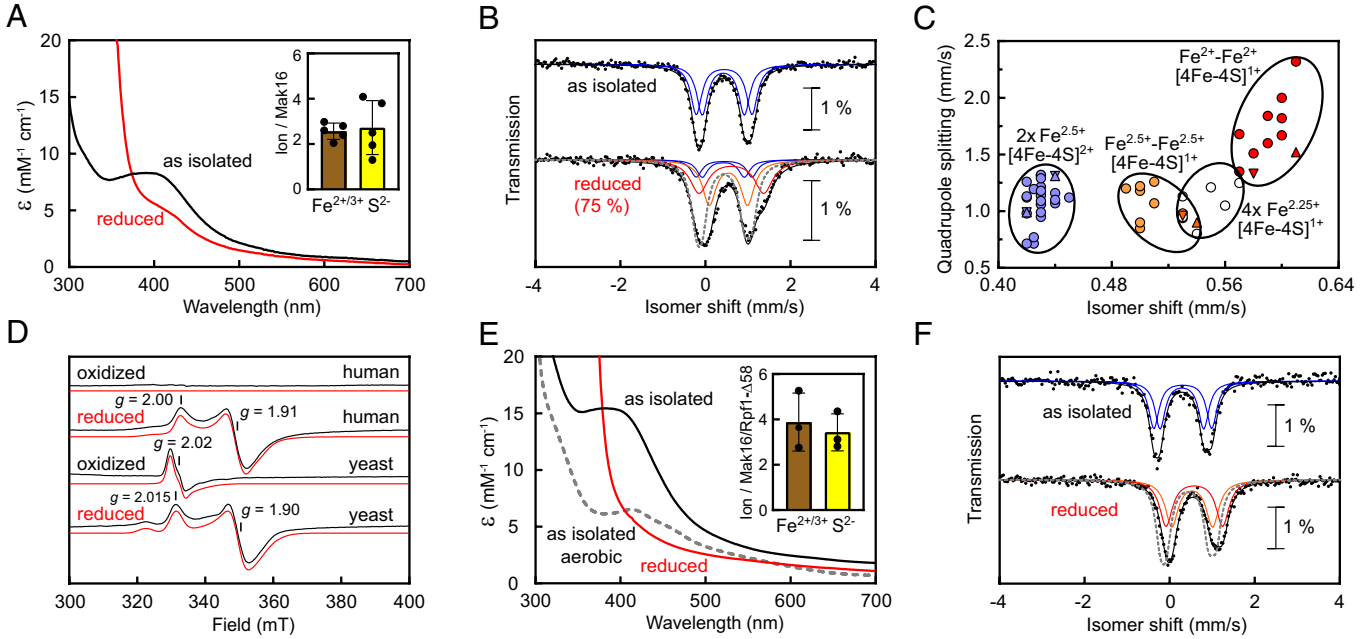


Fig. 2. Yeast and human Mak16 contain a $[4Fe\text{-}4S]^{2+}$ cluster. (*A*) UV-Vis spectrum of anaerobically purified human Mak16 (0.037 mM, black line, as isolated) in 50 mM sodium phosphate, 300 mM NaCl, pH 8.0, and after incubation with 4 mM sodium dithionite (red line, reduced). Inset: Nonheme ($Fe^{2+/3+}$) and acid labile sulfide (S^{2-}) contents (mean ± SEM, n = 5). (*B*) Mössbauer spectra at 77 K in the absence of an applied field of as isolated and partially reduced human Mak16 as in (*A*) but at ~0.4 mM concentration. Fits shown as lines: blue, $[4Fe\text{-}4S]^{2+}$; orange/red, $[4Fe\text{-}4S]^{1+}$; black, sum of components; dotted gray, sum of components for as isolated for comparison. Parameters in *SI Appendix*, Table S1. (*C*) Compilation of Mössbauer parameters for all-cysteine coordinated $[4Fe\text{-}4S]^{2+}$ (blue) and $[4Fe\text{-}4S]^{1+}$ clusters (orange, $Fe^{2.5+}$ pair; red Fe^{2+} pair; open for systems simulated with a single quadrupole doublet); Human Mak16, triangles; yeast Mak16, inverted triangles. Values and references in *SI Appendix*, Tables S2 and S4. (*D*) EPR spectra of 0.5 mM potassium ferricyanide oxidized or 4 mM sodium dithionite treated human Mak16 (0.128 mM) or yeast Mak16/Rpf1-Δ58 complex (0.074 mM). EPR conditions: 9.353 GHz, 10 K, microwave power 0.21 mW. Parameters for simulations (red lines) in *SI Appendix*, Table S3. (*E*) UV-Vis spectrum of anaerobically purified as isolated (black line), dithionite-reduced (red line), and aerobically purified yeast (dashed line) Mak16/Rpf1-Δ58 complex (0.011 mM), as in (*A*). $Fe^{2+/3+}$ and S^{2-} contents for anaerobically purified complex (mean ± SEM, n = 3). (*F*) Mössbauer spectroscopy of anaerobically purified as isolated and reduced yeast Mak16/Rpf1-Δ58 complex (~0.6 mM) as in (*B*).

the Fe/S cluster was highly oxygen-labile: aerobic purification led to a ~50% loss of its chromophore (Fig. 2*E*), underscoring its instability in the presence of oxygen. Though a weak $[3Fe\text{-}4S]^{1+}$ EPR signal (~5%) at g = 2.02 emerged upon oxidation (Fig. 2*D*), the low temperature, high field Mössbauer spectra demonstrated the diamagnetism of the cluster in its as isolated state (*SI Appendix*, Fig. S6*A*). We interpret the low content of a $[3Fe\text{-}4S]^{1+}$ cluster as a product of $[4Fe\text{-}4S]$ cluster degradation. Similar to human Mak16, dithionite treatment resulted in an axial EPR signal with g_z = 2.015 and g_{yx} = 1.90 (Fig. 2*D*, EPR simulation parameters *SI Appendix*, Table S3). Although a minor signal of a S = 3/2 species was detected in highly concentrated dithionite reduced Mak16/Rpf1-Δ58 (*SI Appendix*, Fig. S7), double integration of the simulated spectrum indicated that it accounted for <2% of the intensity relative to the double integral of the g = 2 region. Spin quantification against Cu^{2+} showed that the S = 1/2 EPR signal closely matched the protein concentration (within 5% accuracy). Our findings demonstrate that the $[4Fe\text{-}4S]^{1+}$ cluster is almost exclusively in the S = 1/2 spin state. The Mössbauer spectrum at 77 K was best simulated by two quadrupole doublets with δ_1 = 0.53 mm/s, $\Delta E_{Q,1}$ = 0.96 mm/s and δ_2 = 0.58 mm/s, $\Delta E_{Q,2}$ = 1.33 mm/s, assuming complete reduction to $[4Fe\text{-}4S]^{1+}$. Although magnetic splitting blurred the Mössbauer spectrum at 4 K (*SI Appendix*, Fig. S6*B*), the absence of a central doublet from $[4Fe\text{-}4S]^{2+}$ confirmed the extent of cluster reduction. In summary, heterologously expressed yeast and human Mak16 proteins contain an oxygen-labile $[4Fe\text{-}4S]^{2+/1+}$ cluster.

Disruption of Fe/S Cluster Coordination in Mak16 Strongly Decreases rRNA Levels. Yeast Mak16 is a 306-amino acid protein composed of three domains. The N-terminal region (residues 1 to 128) adopts a knot-like fold that is structurally homologous to ribosomal protein L28e (Fig. 3*A*) and contains four invariant cysteine residues within residues 1 to 48, forming a $CX_{11\text{-}13}CX_9CX_4CP$ consensus motif (*SI Appendix*, Fig. S2*A*), which is consistent with the potential coordination of an Fe/S cluster. The central domain (residues 129 to 191) forms two α-helices that mediate interaction with Rpf1, while the C-terminal region is characterized by alternating stretches of basic and acidic residues. Structural predictions from AlphaFold2 show high agreement with cryo-EM data for the N-terminal and central domains. In contrast, the C-terminal region is predicted to be largely disordered and is absent from all cryo-EM reconstructions (*SI Appendix*, Fig. S8), likely due to its intrinsic flexibility and the limited capacity of cryo-EM to resolve dynamic or unstructured segments. This flexible domain is absent in Mak16 homologues from *Trypanosomatidae* and *Microsporidia*, suggesting that its role in ribosome biogenesis may vary across species.

To analyze the functional importance of the cysteine residues potentially involved in Fe/S cluster coordination, we assessed their role in vivo using the Gal-*MAK16* yeast strain. This strain was transformed with either an empty plasmid, plasmid encoding wild-type Mak16, or cysteine-to-alanine variants expressed under the control of the native *MAK16* promoter. Under permissive conditions (galactose) no obvious growth phenotype was observed (*SI Appendix*, Fig. S9). However, under repressive conditions (glucose) substitutions of Cys28 or Cys43 by alanine resulted in a severe growth defect comparable to empty plasmid control (Fig. 3*B*). Replacement of Cys38 produced an intermediate phenotype, which was further exacerbated by an additional Cys15 substitution (C15A/C38A). In contrast, mutation of the nonconserved Cys55

Downloaded from https://www.pnas.org by Universitaetsbibliothek der RPTU Kaiserslautern-Landau on January 6, 2026 from IP address 131.246.60.80.

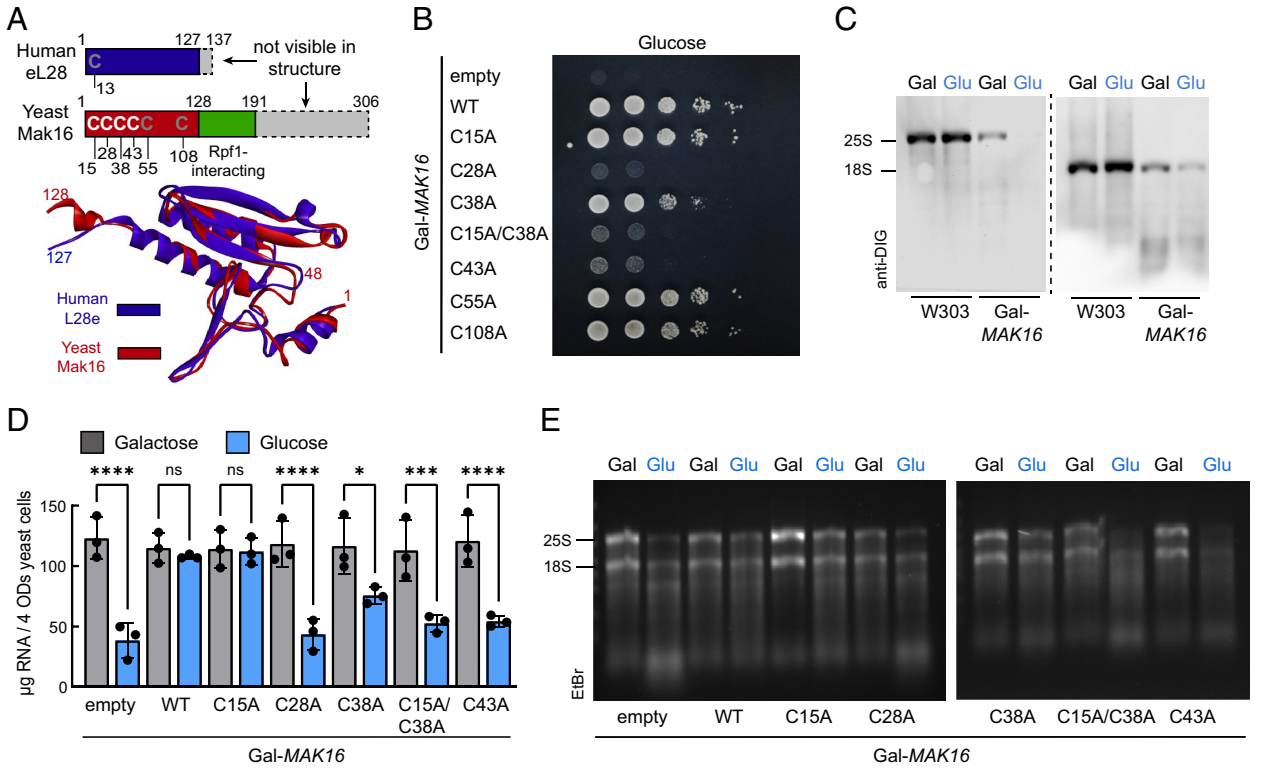


Fig. 3. Disruption of [4Fe-4S] coordination in Mak16 leads to impaired cell growth and rRNA synthesis. (*A*, *Top*) conserved cysteine residues and domain structure of Mak16 in comparison with human L28e. (*Bottom*) Structural alignment of yeast Mak16 (PDB 6EM1) with the human ribosomal protein L28e (PDB 8G5Y). (*B*) Gal-*MAK16* yeast cells, transformed with 416 plasmids under control of the *MAK16* promoter lacking an insert (empty), or encoding wild-type (WT) or cysteine variants of Mak16, were cultured for 16 h in SC medium with glucose. OD-normalized 10-fold serial dilutions were spotted on agar plates of the same medium and photographed after 48 h at 30 °C. (*C*) Northern blots of total RNA isolated from wild-type (W303) and Gal-*MAK16* yeast cells cultivated for 40 h in SC medium with galactose (Gal) or glucose (Glu). rRNA was visualized with digoxigenin-ddUTP labeled 25S (*Left*) or 18S (*Right*) probes and anti-digoxigenin-peroxidase conjugate (*SI Appendix*, Fig. S10). (*D*) Quantification of total RNA isolated from cells grown for 24 h in galactose or glucose containing SC medium, followed by ~6 h of growth to the logarithmic phase. Data are mean value ± SEM ($n = 3$). Significance of differences between groups, as indicated by crossbars, were determined using multiple comparisons one-way ANOVA with Šidák correction (ns, not significant, $^{*}P < 0.05$, $^{***}P < 0.001$, $^{****}P < 0.0001$). (*E*) Total RNA from samples in (*D*) was separated by agarose gel electrophoresis. rRNA bands were visualized with ethidium bromide (*SI Appendix*, Fig. S11).

or Cys108 had no detectable effect. The findings indicate that cysteine residues 15, 28, 38, and 43 within the $CX_{11\text{-}13}CX_9CX_4CP$ consensus motif are essential for coordinating the $[4Fe\text{-}4S]^{2+}$ cluster. Together, these data underscore the critical role of a conserved cysteine-based motif in stabilizing the Fe/S cluster and enabling Mak16 function.

Given that rRNAs constitute the majority of cellular RNA, we examined whether the phenotypic severity of Mak16 cysteine variants (Fig. 3*B*) correlates with total RNA levels. Yeast cells depleted of endogenous Mak16 were harvested during early exponential growth, and total RNA was extracted. In parallel, control RNA was isolated from cells grown in galactose. Northern blotting revealed reduced 25S and, to a lesser extent, 18S rRNA levels upon depletion of wild-type Mak16 (Fig. 3*C* and *SI Appendix*, Fig. S10). Quantitative analysis showed a substantial decrease in total RNA in cells transformed with the empty plasmid (65% reduction), as well as the C28A, C38A, C15A/C38A, and C43A variants (30 to 60% reduction) (Fig. 3*D*). Contrarily, the C15A variant retained wild-type RNA levels. The RNA content paralleled the degree of growth complementation across the different Mak16 variants (Fig. 3 *B* and *D*). Agarose gel electrophoresis showed that both 25S and 18S rRNAs were affected, with 25S rRNA being the most severely impacted (Fig. 3*E*). In conjunction with the ISC/CIA depletion data (Fig. 1 *A*, *C*, and *D*), these findings identify the Fe/S cluster of Mak16 as a critical determinant for proper ribosome biogenesis and thus maintaining cellular rRNA levels.

Mak16/Rpf1 Maintains a Low Redox Potential Independent of Extension Segment 7 (ES7) Binding. Accurate determination of the redox potential of the $[4Fe\text{-}4S]^{2+/1+}$ cluster in both human Mak16 (Fig. 4*A*) and the yeast Mak16/Rpf1-Δ58 complex (Fig. 4*B*) proved challenging. First, the low redox potential of the cluster did prevent full reduction using viologen redox mediators, in contrast to near-complete reduction achieved after a 3-min incubation with sodium dithionite. Second, the chemical lability of the cluster limited the feasibility of prolonged dye-mediated titrations across multiple samples. Nevertheless, EPR spectroscopy unequivocally demonstrates that both human and yeast Mak16 proteins harbor clusters with similarly low redox potentials, estimated to have midpoint potentials near –520 mV vs. the normal hydrogen electrode (NHE). To explore whether rRNA binding modulates the redox properties of Mak16, we examined the interaction between the recombinant yeast Mak16/Rpf1-Δ58 complex and the 25S rRNA ES7, which is associated with Mak16/Rpf1 in cryo-EM structures (16). Electrophoretic mobility shift assays (EMSA) demonstrated the formation of a defined complex upon stoichiometric mixing with in vitro transcribed ES7 (Fig. 4*C*). This interaction resulted in only a slight shift in the midpoint potential from –520 to approximately –500 mV vs. NHE (Fig. 4*D*), indicating that ES7 binding has minimal impact on the redox characteristics of the $[4Fe\text{-}4S]^{2+/1+}$ cluster. Since in the physiology of human and yeast cells there are no redox processes taking place at such low redox potentials,

Downloaded from https://www.pnas.org by Universitaetsbibliothek der RPTU Kaiserslautern-Landau on January 6, 2026 from IP address 131.246.60.80.

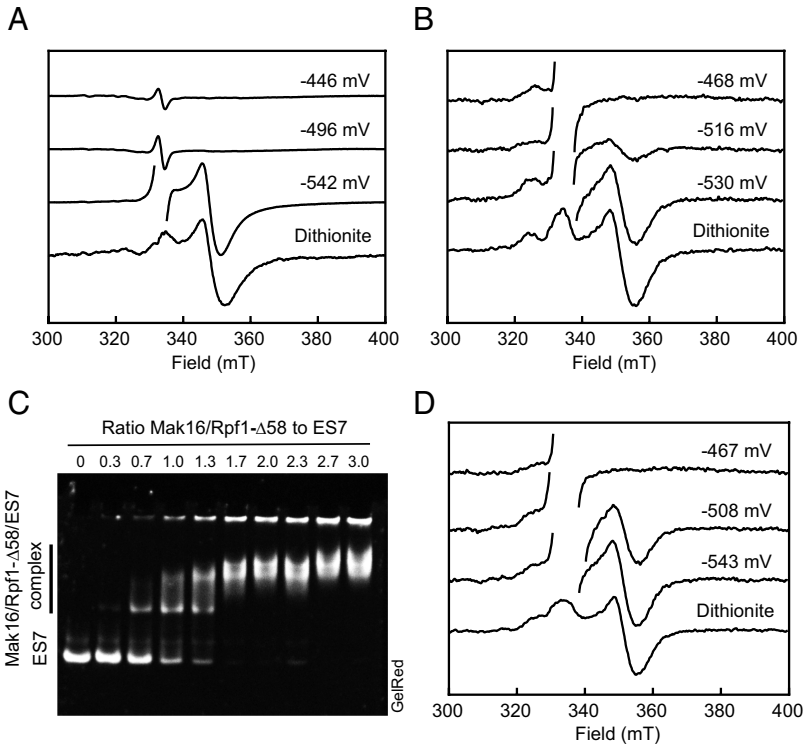


Fig. 4. Redox properties of Mak16. (*A*) EPR-mediated redox titration. Human Mak16 (16 μM) in pyrophosphate buffer pH 9.0 was mixed with redox mediators, and the reduction potential was adjusted with sodium dithionite. EPR spectra for samples taken at indicated potentials are shown. EPR conditions: 9.356 GHz, 10 K, microwave power 0.21 mW. (*B*) EPR-mediated redox titration of yeast Mak16/Rpf1-Δ58 complex (9 μM) as in (*A*). (*C*) Binding of the Mak16/Rpf1 complex to ES7. Purified Mak16/Rpf1-Δ58 was titrated with a fixed amount of ES7 (0.8 μg) in binding buffer. The protein/RNA complex was separated by 5% nondenaturing acrylamide gel electrophoresis, visualized with GelRed and recorded with a gel documentation system. The same gel was further stained with Coomassie dye (*SI Appendix*, Fig. S12). (*D*) Effect of ES7 binding on the redox potential of Mak16/Rpf1 complex. Purified Mak16/Rpf1-Δ58 complex and ES7 (7.3 μM each) were incubated in binding buffer, and subjected to a redox titration as in (*A*).

we propose that Mak16 operates physiologically with its cluster in the $[4Fe\text{-}4S]^{2+}$ state.

Synthetic Lethality Between CIA Machinery Depletion and Expression of the Mak16 C38A Variant. To explore the functional interplay between defective Fe/S cluster coordination in Mak16 and impaired CIA machinery, we explored synthetic lethality effects on cell growth. For this purpose, yeast strains of which both *MAK16* and individual CIA genes were under control of the *GAL* promoter were constructed. Our focus was on the early-acting CIA factors Cfd1, Nbp35, and Cia1, whose depletion is known to produce relatively mild growth defects (29, 30). To probe additive or synergistic effects, we used the Mak16 C38A variant, which exhibits an intermediate growth phenotype in drop tests (Fig. 3*B*). In the Gal-*MAK16* background, the C38A mutation alone led to a growth reduction of approximately two serial dilutions (Fig. 5*A*). However, concurrent depletion of any of the three CIA factors markedly worsened this phenotype, resulting in growth comparable to cells lacking Mak16. These results demonstrate a strong genetic interaction between Mak16 and the CIA pathway, supporting the conclusion that Mak16 depends on an Fe/S cluster delivered via the CIA machinery. This synthetic lethality highlights the essential role of Fe/S cluster incorporation for Mak16 function and emphasizes the broader relevance of CIA-mediated Fe/S protein maturation in ribosome biogenesis.

Destabilization of the Fe/S Cluster Coordination in Mak16 Disrupts Rpf1 Interaction. The in vivo interaction between Mak16 and Rpf1 has been demonstrated through various methods, including high-throughput genetic studies (31), yeast two-hybrid assays (32), in vitro pull-down experiments (33) and cryo-EM structures (16–19, 34). Given the critical role of this interaction for ribosomal maturation, we investigated whether partial or complete abrogation of the Fe/S cluster coordination in Mak16 affects its association with Rpf1. Reciprocal immunoprecipitation in yeast cells depleted of chromosomally encoded Mak16 and Rpf1 (Gal-*MAK16*/Gal-*RPF1*) verified the interaction between plasmid-encoded HA-Mak16 and Myc-Rpf1 proteins (Fig. 5*B*). We then examined a set of Mak16 variants with differing degrees of Fe/S cluster disruption: a nonperturbing variant (C55A), a moderately affected variant (C38A), and two severely affected variants (C28A and C15A/C38A), based on our previous drop test and total RNA quantification data (Fig. 3 *D* and *E*). Both HA-Mak16 and Myc-Rpf1 protein levels were lower in extracts from cells expressing the more severely disrupted variants (C28A, C38A, and C15A/C38A). Notably, the degree of complex formation between Mak16 and Rpf1 correlated with the severity of growth defects (Fig. 3*B*) and decreased total RNA levels: the greater the disruption of Fe/S cluster coordination (i.e., 1 or 2 cysteine residues exchanged to alanine), the more severe the impairment of Mak16/Rpf1 association. These findings demonstrate that proper Fe/S cluster coordination is not only essential for Mak16 structural stability but also for its capacity to engage in functional interactions with Rpf1 during ribosome biogenesis.

Destabilization of the Fe/S Cluster Coordination in Mak16 Increases Sensitivity to Redox Stressors. Previous studies have shown that exposure of yeast cells to sublethal doses of reactive oxygen species (ROS) generating agents leads to cleavage of 25S

Downloaded from https://www.pnas.org by Universitaetsbibliothek der RPTU Kaiserslautern-Landau on January 6, 2026 from IP address 131.246.60.80.

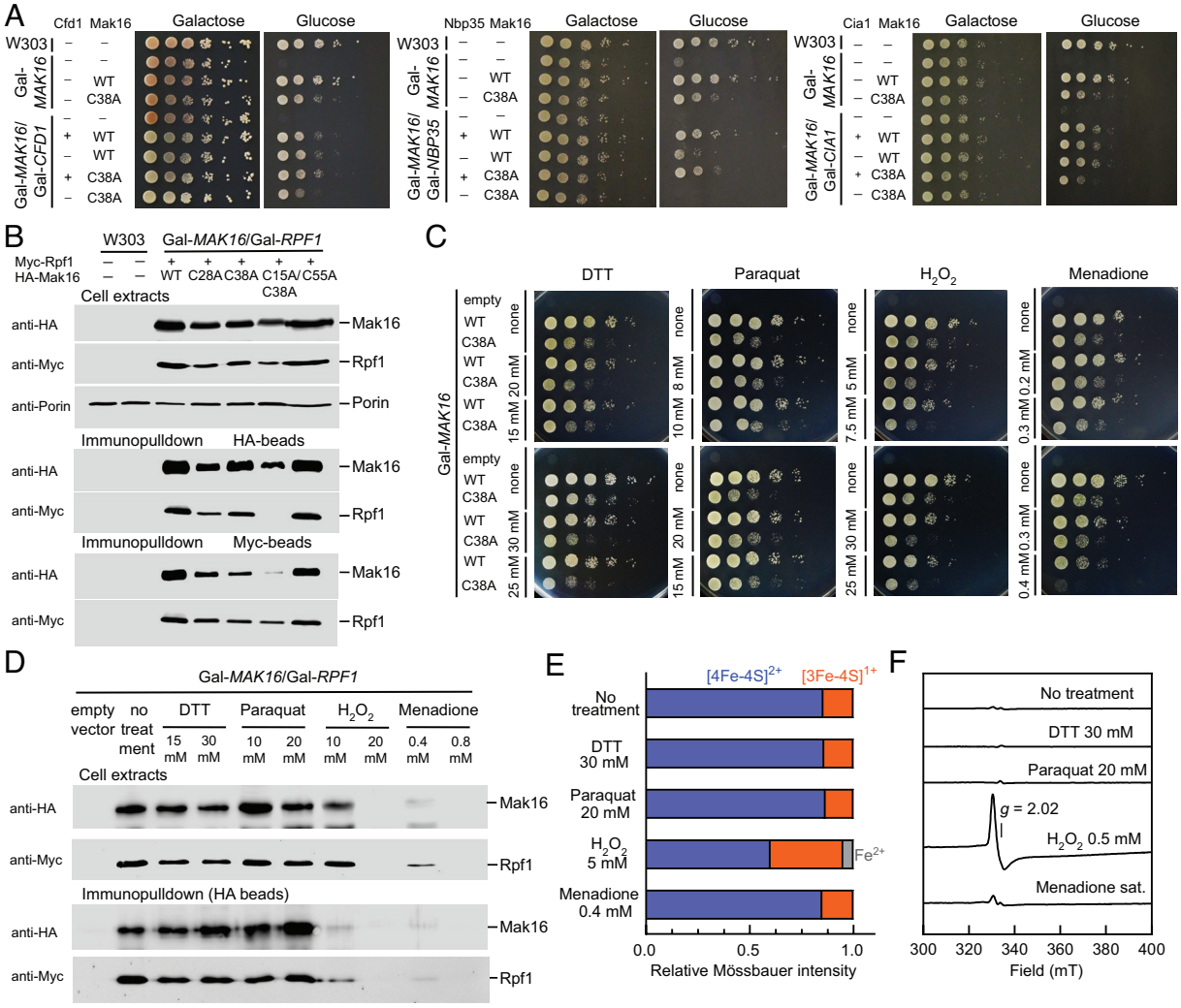


Fig. 5. Effect of redox stressors on wild type Mak16, its C38A variant and Rpf1 binding. (*A*) Synthetic lethality between CIA machinery depletion and the Mak16 C38A variant. Indicated yeast strains were transformed with an empty, WT Mak16, or C38A Mak16 variant encoding plasmid, along with an empty plasmid or plasmid encoding the indicated CIA factor. After 16 h of growth on galactose or glucose, 10-fold serial dilutions were spotted on SC agar galactose or glucose plates and photographed after 48 h at 30 °C. (*B*) Disruption of Fe/S coordination in Mak16 impairs its interaction with Rpf1. W303 without plasmids or the Gal-*MAK16*/Gal-*RPF1* strain transformed with plasmids encoding WT or cysteine variants of HA-Mak16 and Myc-Rpf1 were grown for 40 h on glucose. Immunoprecipitates of cell extracts with either HA or Myc beads were subjected to western blot analysis with indicated antibodies (*SI Appendix*, Fig. S13). (*C*) Conditional lethality caused by expression of the Mak16 C38A variant and treatment with redox stressors. Gal-*MAK16* cells transformed with an empty plasmid, or a plasmid encoding WT, or the C38A Mak16 variant were grown on SC glucose for 16 h, then treated 2 h with indicated redox stressors, and 10-fold serial dilutions were spotted on SC glucose agar plates. After 48 h of growth at 30 °C plates were photographed. (*D*) Disruption of Fe/S of WT Mak16 by stressors in vivo impairs its stability and interaction with Rpf1. Gal-*MAK16*/Gal-*RPF1* cells transformed with empty plasmids or plasmids encoding WT HA-Mak16 and Myc-Rpf1 were grown and processed as in (*B*). Full blots in *SI Appendix*, Fig. S14. (*E*) Relative intensities of the quadrupole doublets at 77 K in the Mössbauer spectra (*SI Appendix*, Fig. S15) of purified ^{57}Fe-enriched Mak16/Rpf1-Δ58 after treatment with indicated compounds (30 min., 23 °C). The sample used had a higher $[3Fe\text{-}4S]^{1+}$ content than that in Fig. 2*F*. (*F*) EPR spectra of purified Mak16/Rpf1-Δ58 frozen after treatment with indicated compounds (30 min, 23 °C). EPR conditions: 9.352 GHz, 10 K, microwave power 0.21 mW.

rRNA, particularly in the c-loop of ES7 (35). In the experiments dithiothreitol (DTT) was also included, which, despite its common use as a stabilizing agent, by reaction with O_2 increased the level of H_2O_2 in yeast (35). Interestingly, not ROS itself, but the presence of redox-active iron present in the ribosomes specifically contributed to destabilization of 25S rRNA through an unknown mechanism (36). The origin of free iron in the ribosomes was unclear, but was increased in cells lacking Grx5 (37). In this context, RNA cleavage was detected not only in 25S, but also observed in 18S, 5.8S, and 5S rRNA. Given that Mak16 harbors a redox-active [4Fe-4S] cluster and interacts extensively with ES7a, while being in proximity to ES7c, we tested the impact of destabilization of the Fe/S coordination in Mak16 on cells exposed to the redox stressors from the ES7 cleavage screen (H_2O_2, menadione, and DTT), supplemented by the superoxide generating compound paraquat. Since cells lacking Mak16 are nonviable, precluding the observation of any secondary phenotypes, we employ the sensitized Mak16 variant C38A, which already proved suitable in synthetic lethality assays with CIA depletion (Fig. 5*A*). Among the four agents tested, paraquat up to 20 mM had no discernible effect on growth of cells expressing wild type Mak16 or the C38A variant, with viability comparable to untreated controls (Fig. 5*C*). In contrast, DTT and hydrogen peroxide (H_2O_2) significantly decreased growth, indicating increased sensitivity to redox stress. Menadione elicited the strongest response causing a markedly greater effect than the other treatments. These results suggest that Mak16 and its C38A variant are vulnerable to ROS challenge, particularly quinone-induced stress. So we essentially reproduced a phenotype induced by the ROS agents previously described (35–37). In our cells, however, the observed growth effect was

Downloaded from https://www.pnas.org by Universitaetsbibliothek der RPTU Kaiserslautern-Landau on January 6, 2026 from IP address 131.246.60.80.

not related to an increased ferrous iron concentration in the cytoplasm but rather linked to the destabilization of the Fe/S cluster coordination in Mak16, potentially leading to release of free Fe^{2+} upon Fe/S cluster breakdown. The specific relationship between the observed cleavage sites (37) and iron released from the degradation of Fe/S on Mak16 remains, however, to be elucidated. A plausible explanation is that destabilization of the Fe/S cluster in Mak16 results in the release of free Fe^{2+}, which may locally associate with rRNA. In an oxidative environment, this redox-active iron could facilitate site-specific RNA damage through Fenton-type reactions, particularly at exposed vulnerable structural regions such as ES7.

Wild type Mak16 Is Sensitive to Oxidative Stress. The growth phenotypes observed in sensitized cells (Fig. 5*C*) could, in principle, reflect effects on other essential Fe/S proteins or be specific to the C38A variant. To address this and capture the physiologically relevant situation in which all four cysteines coordinate the [4Fe–4S] cluster, we examined whether treatment with hydrogen peroxide, menadione, DTT, or paraquat affects the stability of wild type Mak16 and its interaction with Rpf1. DTT treatment did not alter Mak16 levels or Rpf1 binding (Fig. 5*D*), and paraquat likewise had no effect. In contrast, hydrogen peroxide and menadione caused a pronounced decrease in Mak16 abundance and in coprecipitated Rpf1, indicating destabilization of the Mak16–Rpf1 complex. The discrepancy between the mild growth phenotype and the lack of effect in pulldowns suggests that DTT may exert pleiotropic effects unrelated to Mak16. Although it is impossible to prove that H_2O_2 and menadione act solely via loss of Mak16 function to impair growth, the combined data (Fig. 5 *C* and *D*) strongly support the notion that Mak16 and the Fe/S protein Rli1 (38) are cytosolic Achilles' heels of eukaryotes regarding oxidative stress.

To further investigate the intrinsic sensitivity of the Mak16 Fe/S cluster, we analyzed the purified ^{57}Fe-enriched Mak16/Rpf1-Δ58 complex under defined stress conditions. Mössbauer spectroscopy revealed that DTT and menadione caused less than 5% loss of the $[4Fe\text{-}4S]^{2+}$ cluster under anaerobic conditions, whereas hydrogen peroxide induced substantial cluster degradation, with formation of a $[3Fe\text{-}4S]^{1+}$ species, confirmed by an EPR signal at $g = 2.02$ (Fig. 5 *E* and *F* and *SI Appendix,* Fig. S15). While menadione produces a strong phenotype in vivo, it had no direct effect on the Fe/S cluster in vitro, because in the absence of cellular redox systems, oxygen, and electron donors required for redox cycling, it cannot generate ROS and therefore cannot chemically react with the cluster. These findings indicate that menadione-induced damage in vivo arises entirely from intracellular ROS generation, rather than direct cluster destabilization. Taken together, these results establish that the wild-type Mak16 Fe/S cluster is intrinsically sensitive to oxidative stress. Hydrogen peroxide causes direct cluster breakdown, menadione highlights the contribution of intracellular ROS pathways, and the mild DTT effect observed in growth assays arises from secondary, indirect ROS formation. Paraquat has no measurable impact under either experimental context.

Discussion

Our investigation into Mak16 was motivated by its consistent copurification with components of the CIA-targeting complex, which mediates the final delivery of Fe/S clusters to recipient proteins (20, 21). We were equally intrigued by the observation that a yeast allele leading to a change of a conserved cysteine residue (C38Y) of Mak16 exhibited defects in 60S ribosomal subunit maturation (39). Nevertheless, subsequent cryo-EM analyses of Mak16 in yeast preribosomal particles either lacked a metal cofactor (16, 18) or showed a Zn^{2+} ion (17, 19). More extensive electron density was reported only in human Mak16 at higher resolution, where it was provisionally modeled as an Fe/S cluster, though without validation (34). In this study, we present robust evidence that yeast Mak16 is a bone fide [4Fe-4S] protein. We further characterized the biophysical properties of both yeast and human Mak16, and define the in *vivo* significance of its Fe/S cluster in yeast Mak16 in the context of ribosome biogenesis.

To directly address the apparent discrepancies in metal cofactor assignment and to establish the relevance of an Fe/S cluster in Mak16, we employed the gold-standard ^{55}Fe radiolabeling assay to assess the incorporation of ^{55}Fe into affinity-tagged HA-Mak16 (Fig. 1*A*). Although ^{55}Fe binding alone does not definitively establish the presence of a physiologically relevant Fe/S cluster, this observation, combined with the strict dependence on Nfs1, the essential mitochondrial cysteine desulfurase of the iron–sulfur cluster (ISC) assembly machinery, provides compelling evidence for an Fe/S cluster of Mak16 in vivo. Furthermore, efficient ^{55}Fe incorporation into Mak16 required the CIA components Nar1 and Cia2, underscoring the importance of both the ISC and CIA pathways in its maturation. These results collectively demonstrate that Mak16 is a genuine Fe/S protein whose cluster biogenesis depends on the canonical cellular Fe/S machineries.

To further explore the phylogenetic conservation of Fe/S clusters in Mak16, we expanded our analysis to include two unicellular eukaryotic parasites with highly divergent cellular and metabolic adaptations: *T. brucei* and *E. cuniculi*. We demonstrated that Mak16 from both organisms, when expressed in yeast, also harbors an Fe/S cluster (Fig. 1*B*). In *T. brucei*, the causative agent of African trypanosomiasis (sleeping sickness), Mak16 thus appears to be an important client of both the ISC and CIA machineries, highlighting the essential role of Fe/S cluster biogenesis in this pathogen (40–42). Interestingly, tryptophan is the C-terminal amino acid residue of Mak16 proteins from *T. brucei*, *E. cuniculi*, and nearly all other trypanosomal and microsporidial species (*SI Appendix,* Fig. S16). Analysis of 1,900 eukaryotic Mak16 proteins reveals that 17% has tryptophan as C-terminus, a 14-fold enrichment when corrected for the abundance of tryptophan. The tryptophan is part of the consensus sequence [LIM]-[DES]-[WF], a motif known to recruit the CIA targeting complex in approximately 25% of all eukaryotic cytosolic and nuclear Fe/S proteins (43). In contrast, both yeast and human Mak16 lack this sequence, suggesting that in these organisms Mak16 may rely on an internal recognition sequence or employs a dedicated adaptor protein for recruiting the CIA targeting complex. Although the involvement of the CIA machinery in Mak16 maturation is established, several key questions remain, including whether Mak16 interacts with the CIA targeting complex only before and during cluster assembly, how its release is coordinated, and whether cluster insertion occurs prior to or following nuclear import.

We focused then on the biophysical properties of recombinant yeast and human Mak16 proteins (Fig. 2). Comprehensive characterization of human Mak16 and the yeast Mak16/Rpf1-Δ58 complex using EPR and Mössbauer spectroscopy revealed a $[4Fe\text{-}4S]^{2+/1+}$ cluster in Mak16. The EPR and Mössbauer features of Mak16 closely resemble those observed for tetracysteinyl coordinated protein-bound $[4Fe\text{-}4S]^{2+/1+}$ clusters (28, 44). EPR-monitored redox titrations in solution demonstrated that the $[4Fe\text{-}4S]^{2+/1+}$ cluster exhibits a low midpoint potential of approximately –520 mV vs. NHE (Fig. 4 *A* and *B*). This potential is lower than that of [4Fe-4S] clusters of the bacterial ferredoxin type with typical midpoint potentials between –480 and –400 mV

Downloaded from https://www.pnas.org by Universitaetsbibliothek der RPTU Kaiserslautern-Landau on January 6, 2026 from IP address 131.246.60.80.

vs. NHE (45, 46). A key question was whether recombinant purified Mak16/Rpf1-Δ58 complex could bind its 25S rRNA interaction sequences, specifically the expansion segment 7 (ES7), a 210-nucleotide sequence that, according to high-resolution cryo-EM, adopts a characteristic L-shaped fold (16–19). This structure facilitates interaction with the Mak16 (or Nsa1) module, comprising Mak16, Rpf1, Nsa1, and Rrp1, clamping rRNA domains I and II during 60S ribosome assembly. EMSA analysis demonstrated stoichiometric binding between the Mak16/Rpf1-Δ58 complex and synthetic ES7 (Fig. 4*C*), establishing a critical prerequisite for subsequent evaluation of the redox properties of yeast Mak16 upon RNA binding. Under the conditions used for EMSA, the Mak16/Rpf1-Δ58/ES7 complex exhibited, if any, only a 20 mV upshift of the midpoint potential in solution as revealed by EPR spectroscopy (Fig. 4*D*). Such minimal shift cannot cause a relevant change of ES7 binding to the Mak16/Rpf1 complex at the prevalent glutathione and NADP(H) based potential of ~–300 mV in the eukaryotic cell (47). Therefore, Mak16 functions in ribosome biogenesis with its cluster in the $[4Fe\text{-}4S]^{2+}$ state, which we consider to be its biologically active form. In contrast, studies on replicative polymerases and other DNA-interacting proteins have demonstrated that their binding to DNA induces a significant redox potential shift in their [4Fe-4S] clusters (48). Notably, these studies employed DNA-modified surfaces for cyclic voltammetry and are fundamentally different from electrochemical methods in bulk solution. Taken together, our results indicated that, while the interaction with ES7 is crucial for Mak16 function, the redox state of the Fe/S cluster does not modulate ES7 binding.

On other hand, our data demonstrated that the solvent-exposed [4Fe-4S] cluster of Mak16 is highly susceptible to breakdown under aerobic conditions or oxidative stress. Upon breakdown ferrous iron (Fe^{2+}) is released, which via Fenton chemistry can generate hydroxyl radicals ($^{\bullet}OH$) capable of not only damaging DNA, but also RNA (49). Under redox stress, yeast expressing the C38A variant showed stronger growth defects than wild-type, indicating that 25S rRNA maturation requires an intact Fe/S cluster. Moreover, this finding mirrors the phenotype of the *mak16-1* allele described by Pellett and Tracy (39), in which substitution of Cys38 with tyrosine impaired 60S ribosome biogenesis. We therefore examined the functional consequences of cysteine variants of Mak16 in yeast cells. In the variants of the Fe/S cluster coordinating cysteine residues, levels of both Mak16 and its binding partner Rpf1 were decreased (Fig. 5*B*). Importantly, the cellular level of Mak16 correlated with the severity of observed phenotypes, including defects in cell viability, decreased rRNA synthesis, and disruption of the Mak16/Rpf1 complex. Phenotypic outcomes ranged from unaltered growth for the C15A variant, to moderate growth defects for C38A, and to complete growth arrest in C28A, C43A, and C15A/C38A variants (Fig. 3*B*). The total RNA yields, largely composed of rRNA, mirrored this gradient of severity (Fig. 3*D*). These results indicate the following scenario: disruption of Fe/S cluster coordination compromises Mak16 stability, impairs binding to Rpf1, leading to defective ribosome biogenesis, and ultimately loss of cell viability. Why is the Fe/S cluster of Mak16 so critical for 60S ribosomal subunit maturation? Cryo-EM structures have shown that the NTD of Mak16 containing the cluster binding cysteine residues is positioned at the core of a ribonucleoprotein pocket of the 25S rRNA hairpins 45 and 46, and the ribosomal proteins L4 and L32 (16, 18). The central domain of Mak16 is in close contact with ES7 and engages the Brix-domain-containing assembly factor Rpf1, which also contacts the basal part of ES7. Given that the Fe/S cluster is embedded within the NTD, its disruption likely induces severe conformational changes of Mak16 compromising the coordinated interactions with Rpf1 and rRNA. Consequently, destabilization or disruption of the Fe/S cluster impairs early 60S ribosomal subunit maturation.

To assess the consequences of impaired Fe/S cluster biogenesis of Mak16, we quantified total RNA levels in yeast strains depleted of Nfs1, Nar1, and Cia2, essential components of the ISC and CIA pathways. Depletion of these factors led to a significant decrease in total rRNA levels, with the 25S rRNA exhibiting the most pronounced reduction (Fig. 1 *C* and *D*). The consistent phenotypic severity of Mak16 cysteine variants (Fig. 3 *B* and *D*), which mimic the effects of impaired Fe/S cluster biogenesis, strongly indicate that the observed defects are specific to Mak16. This link was reinforced by synthetic lethality observed in strains expressing the C38A Mak16 variant in combination with depletion of the CIA components Cfd1, Nbp35, and Cia1 (Fig. 5*A*). Together, these findings underscore the essential role of the Fe/S cluster assembly machinery in maintaining Mak16 function, coordinating ribosome biogenesis, and ensuring cell viability. Extending beyond established roles in genome maintenance and translation (2), our findings now implicate Fe/S cluster biogenesis in one of the most fundamental steps in protein synthesis: the maturation of the large ribosomal subunit.

Building on the crucial role of Fe/S cluster biogenesis in ribosome maturation, it is important to consider the impact of redox stress on Mak16 function. Given its sensitivity (Figs. 2*E* and 5 *C*–*E*), it is plausible that Mak16 is an "Achilles' heel" under oxidative stress conditions. This terminology has been applied to the Rli1 protein, which possesses two [4Fe-4S] clusters highly sensitive to oxidative stress (38, 50, 51). Current studies describe translation termination and ribosome recycling as primary functions of Rli1 (5). Rli1 (ABCE1 in humans) also functions in the "test driving" of the pre-40S or pre-60S particles in a cytoplasmic translation-like quality control step (52), but not directly in ribosomal maturation per se (34, 53). This mechanism echoes observations in mitochondrial translation, where the solvent-exposed [4Fe-4S] cluster of the mitoribosomal assembly factor METTL17 is destabilized by oxidative stress, leading to cluster loss and arrested mitoribosomal translation (9, 54). Not only the Fe/S cluster of METTL17, but also two of the three structural [2Fe-2S] clusters of the human mitochondrial ribosome (7, 8) are highly sensitive to H_2O_2 and their disruption impairs mitochondrial translation (54, 55). Mak16, Rli1, and the mitoribosomal Fe/S proteins underscore a conserved principle: even when Fe/S clusters do not mediate redox chemistry, they supply a redox sensing capability which allows to sense oxidative stress and attenuate translation. In conclusion, we identify Mak16 as a redox-sensitive Fe/S protein essential for 60S ribosomal subunit maturation. Our findings show that its [4Fe-4S] cluster, synthesized through the ISC and CIA pathways, plays a critical role in stabilizing Mak16 and facilitating its complex formation with the partner protein Rpf1. We propose that the redox sensitivity of the cluster enables Mak16 to function as a sensor for redox stress conditions, modulating ribosome biogenesis.

Materials and Methods

Detailed descriptions of yeast and *E. coli* strains, growth conditions, complementation assays, cloning and mutagenesis procedures, western blotting, ^{55}Fe incorporation assays, and protein–protein interaction studies in yeast cells are provided in the *SI Appendix*. Additional methods for overexpression and purification, as well as UV-Vis, EPR and Mössbauer spectroscopic characterization of yeast and human Mak16, are also described in the *SI Appendix*. RNA-related experiments, including RNA isolation, Northern blotting, synthesis of ES7 RNA, and electrophoretic mobility shift assays (EMSAs), are likewise detailed in the *SI Appendix*. Statistical analyses and reproducibility measures were performed

Downloaded from https://www.pnas.org by Universitaetsbibliothek der RPTU Kaiserslautern-Landau on January 6, 2026 from IP address 131.246.60.80.

with GraphPad Prism 9. Graphical data are presented as mean ± SEM. Statistical significance was assessed using multiple comparisons one-way ANOVA with Šidák correction. Mössbauer spectra were simulated with Lorentzian lineshapes in Microsoft Office Excel 2019, and Vinda for spectra recorded with applied fields (56, 57). EPR spectra were simulated with Gstrain5 (58). Structural alignment was performed with BIOVIA Discovery Studio 2024.

Data, Materials, and Software Availability. All data have been deposited at Zenodo (59). All other data are included in the article and/or *SI Appendix*.

ACKNOWLEDGMENTS. This research was supported by the funded by the Deutsche Forschungsgemeinschaft (DFG, German Research Foundation), grant number 389965693 (to D.J.N.) and the SPP 1927 Iron-Sulfur for Life project number 311771359 (to A.J.P.) and 311771384 (to V.S.). The upgrade of the EPR spectrometer and closed-cycle cryostat (A.J.P.) was funded by the government of Rhineland-Palatinate and the DFG (248/320-1, project number 444947649). We thank Tamara Roth and Larissa Schatteburg for help at the early phase of the project. In addition, V.S. acknowledges the support of the Rhineland-Palatinate research initiative NanoKat.

Author affiliations: [a]Department of Chemistry, Rheinland-Pfälzische Technische Universität Kaiserslautern-Landau, Kaiserslautern 67663, Germany; [b]Department of Physics, Rheinland-Pfälzische Technische Universität Kaiserslautern-Landau, Kaiserslautern 67663, Germany; and [c]Institut für Zytobiologie und Zytopathologie, Fachbereich Medizin und Zentrum für Synthetische Mikrobiologie Synmikro, Philipps-Universität Marburg, Marburg 35032, Germany

1. D. C. Johnson, D. R. Dean, A. D. Smith, M. K. Johnson, Structure, function, and formation of biological iron-sulfur clusters. *Annu. Rev. Biochem.* **74**, 247–281 (2005).
2. J. O. Fuss, C.-L. Tsai, J. P. Ishida, J. A. Tainer, Emerging critical roles of Fe-S clusters in DNA replication and repair. *Biochim. Biophys. Acta* **1853**, 1253–1271 (2015).
3. M. Girbig *et al.*, Cryo-EM structures of human RNA polymerase III in its unbound and transcribing states. *Nat. Struct. Mol. Biol.* **28**, 210–219 (2021).
4. B. J. Greber, D. B. Toso, J. Fang, E. Nogales, The complete structure of the human TFIIH core complex. *Elife* **8**, e44771 (2019).
5. D. J. Young, N. R. Guydosh, F. Zhang, A. G. Hinnebusch, R. Green, Rli1/ABCE1 recycles terminating ribosomes and controls translation reinitiation in 3′UTRs in vivo. *Cell* **162**, 872–884 (2015).
6. E. Nürenberg-Goloub *et al.*, Molecular analysis of the ribosome recycling factor ABCE1 bound to the 30S post-splitting complex. *EMBO J.* **39**, e103788 (2020).
7. Y. Itoh *et al.*, Structure of the mitoribosomal small subunit with streptomycin reveals Fe-S clusters and physiological molecules. *Elife* **11**, e77460 (2022).
8. V. Singh *et al.*, Mitoribosome structure with cofactors and modifications reveals mechanism of ligand binding and interactions with L1 stalk. *Nat. Commun.* **15**, 4272 (2024).
9. T. Ast *et al.*, METTL17 is an Fe-S cluster checkpoint for mitochondrial translation. *Mol. Cell* **84**, 359–374 (2024).
10. J. Baßler, E. Hurt, Eukaryotic ribosome assembly. *Annu. Rev. Biochem.* **88**, 281–306 (2019).
11. S. Klinge, J. L. Woolford, Ribosome assembly coming into focus. *Nat. Rev. Mol. Cell Biol.* **20**, 116–131 (2019).
12. A. Vanden Broeck, S. Klinge, Eukaryotic ribosome assembly. *Annu. Rev. Biochem.* **93**, 189–210 (2024).
13. D. J. Klein, P. B. Moore, T. A. Steitz, The contribution of metal ions to the structural stability of the large ribosomal subunit. *RNA* **10**, 1366–1379 (2004).
14. M. Laitaoja, J. Valjakka, J. Jänis, Zinc coordination spheres in protein structures. *Inorg. Chem.* **52**, 10983–10991 (2013).
15. M. Ameismeier *et al.*, Structural basis for the final steps of human 40S ribosome maturation. *Nature* **587**, 683–687 (2020).
16. L. Kater *et al.*, Visualizing the assembly pathway of nucleolar pre-60S ribosomes. *Cell* **171**, 1599–1610 (2017).
17. Z. A. Sanghai *et al.*, Modular assembly of the nucleolar pre-60S ribosomal subunit. *Nature* **556**, 126–129 (2018).
18. D. Zhou *et al.*, Cryo-EM structure of an early precursor of large ribosomal subunit reveals a half-assembled intermediate. *Protein Cell* **10**, 120–130 (2019).
19. Z. A. Sanghai, R. Piwowarczyk, A. V. Broeck, S. Klinge, A co-transcriptional ribosome assembly checkpoint controls nascent large ribosomal subunit maturation. *Nat. Struct. Mol. Biol.* **30**, 594–599 (2023).
20. O. Stehling *et al.*, Human CIA2A-FAM96A and CIA2B-FAM96B integrate iron homeostasis and maturation of different subsets of cytosolic-nuclear iron-sulfur proteins. *Cell Metab.* **18**, 187–198 (2013).
21. O. Stehling *et al.*, MMS19 assembles iron-sulfur proteins required for DNA metabolism and genomic integrity. *Science* **337**, 195–199 (2012).
22. A. J. Pierik, D. J. A. Netz, R. Lill, Analysis of iron-sulfur protein maturation in eukaryotes. *Nat. Protoc.* **4**, 753–766 (2009).
23. D. J. Netz *et al.*, Eukaryotic DNA polymerases require an iron-sulfur cluster for the formation of active complexes. *Nat. Chem. Biol.* **8**, 125–132 (2011).
24. J. J. Braymer, S. A. Freibert, M. Rakwalska-Bange, R. Lill, Mechanistic concepts of iron-sulfur protein biogenesis in biology. *Biochim. Biophys. Acta Mol. Cell Res.* **1868**, 118863 (2021).
25. J. Balk, A. J. Pierik, D. J. A. Netz, U. Mühlenhoff, R. Lill, The hydrogenase-like Nar1p is essential for maturation of cytosolic and nuclear iron–sulphur proteins. *EMBO J.* **23**, 2105–2115 (2004).
26. U. Mühlenhoff *et al.*, Functional characterization of the eukaryotic cysteine desulfurase Nfs1p from *Saccharomyces cerevisiae*. *J. Biol. Chem.* **279**, 36906–36915 (2004).
27. J. R. Warner, The economics of ribosome biosynthesis in yeast. *Trends Biochem. Sci.* **24**, 437–440 (1999).
28. M.-E. Pandelia, N. D. Lanz, S. J. Booker, C. Krebs, Mössbauer spectroscopy of Fe/S proteins. *Biochim. Biophys. Acta* **1853**, 1395–1405 (2015).
29. D. J. A. Netz, A. J. Pierik, M. Stümpfig, U. Mühlenhoff, R. Lill, The Cfd1-Nbp35 complex acts as a scaffold for iron-sulfur protein assembly in the yeast cytosol. *Nat. Chem. Biol.* **3**, 278–286 (2007).
30. J. Balk, D. J. Netz, M. Stümpfig, U. Mühlenhoff, R. Lill, The essential WD40 protein Cia1 is involved in a late step of cytosolic and nuclear iron-sulfur protein assembly. *Mol. Cell. Biol.* **25**, 10833–10841 (2005).
31. M. Costanzo *et al.*, A global genetic interaction network maps a wiring diagram of cellular function. *Science* **353**, aaf1420 (2016).
32. K. L. McCann, J. M. Charette, N. G. Vincent, S. J. Baserga, A protein interaction map of the LSU processome. *Genes Dev.* **29**, 862–875 (2015).
33. J. Baßler *et al.*, Interaction network of the ribosome assembly machinery from a eukaryotic thermophile. *Protein Sci.* **26**, 327–342 (2017).
34. A. Vanden Broeck, S. Klinge, Principles of human pre-60S biogenesis. *Science* **381**, eadh3892 (2023).
35. D. Shedlovskiy, J. A. Zinskie, E. Gardner, D. G. Pestov, N. Shcherbik, Endonucleolytic cleavage in the expansion segment 7 of 25S rRNA is an early marker of low-level oxidative stress in yeast. *J. Biol. Chem.* **292**, 18469–18485 (2017).
36. J. A. Zinskie *et al.*, Iron-dependent cleavage of ribosomal RNA during oxidative stress in the yeast *Saccharomyces cerevisiae*. *J. Biol. Chem.* **293**, 14237–14248 (2018).
37. D. G. J. Smethurst, N. Kovalev, E. R. McKenzie, D. G. Pestov, N. Shcherbik, Iron-mediated degradation of ribosomes under oxidative stress is attenuated by manganese. *J. Biol. Chem.* **295**, 17200–17214 (2020).
38. A. Alhebshi, T. C. Sideri, S. L. Holland, S. V. Avery, The essential iron-sulfur protein Rli1 is an important target accounting for inhibition of cell growth by reactive oxygen species. *Mol. Biol. Cell* **23**, 3582–3590 (2012).
39. S. Pellett, J. W. Tracy, Mak16p is required for the maturation of 25S and 5.8S rRNAs in the yeast *Saccharomyces cerevisiae*. *Yeast* **23**, 495–506 (2006).
40. S. Basu *et al.*, Cytosolic iron-sulphur protein assembly is functionally conserved and essential in procyclic and bloodstream *Trypanosoma brucei*. *Mol. Microbiol.* **93**, 897–910 (2014).
41. M. L. Tonini *et al.*, Branched late-steps of the cytosolic iron-sulphur cluster assembly machinery of *Trypanosoma brucei*. *PLoS Pathog.* **14**, e1007326 (2018).
42. T. A. Dellibovi-Ragheb, J. E. Gisselberg, S. T. Prigge, Parasites fes up: Iron-sulfur cluster biogenesis in eukaryotic pathogens. *PLoS Pathog.* **9**, e1003227 (2013).
43. M. D. Marquez *et al.*, Cytosolic iron-sulfur protein assembly system identifies clients by a C-terminal tripeptide. *Proc. Natl. Acad. Sci. U.S.A.* **120**, e2311057120 (2023).
44. M. Belinskii, Spin coupling model for tetrameric iron clusters in ferredoxins. I. Theory, exchange levels, *g*-factors. *Chem. Phys.* **172**, 189–211 (1993).
45. R. Cammack, K. K. Rao, D. O. Hall, Metalloproteins in the evolution of photosynthesis. *Bio Syst.* **14**, 57–80 (1981).
46. L. Valer *et al.*, Methods to identify and characterize iron–sulfur oligopeptides in water. *Can. J. Chem.* **100**, 475–483 (2022).
47. M. Kwolek-Mirek *et al.*, Strategies to maintain redox homeostasis in yeast cells with impaired fermentation-dependent NADPH generation. *Int. J. Mol. Sci.* **25**, 9296 (2024).
48. J. K. Barton, R. M. B. Silva, E. O'Brien, Redox chemistry in the genome: Emergence of the 4Fe4S cofactor in repair and replication. *Annu. Rev. Biochem.* **88**, 163–190 (2019).
49. N. Shcherbik, D. G. Pestov, The impact of oxidative stress on ribosomes: From injury to regulation. *Cells* **8**, 1379 (2019).
50. A. Yarunin *et al.*, Functional link between ribosome formation and biogenesis of iron-sulfur proteins. *EMBO J.* **24**, 580–588 (2005).
51. G. Kispal *et al.*, Biogenesis of cytosolic ribosomes requires the essential iron-sulphur protein Rli1p and mitochondria. *EMBO J.* **24**, 589–598 (2005).
52. J. L. Woolford, S. J. Baserga, Ribosome biogenesis in the yeast *Saccharomyces cerevisiae*. *Genetics* **195**, 643–681 (2013).
53. E. Hurt, J. Iwasa, R. Beckmann, Snapshot: Eukaryotic ribosome biogenesis II. *Cell* **187**, 1314–1314 (2024).
54. H. Zhong *et al.*, BOLA3 and NFU1 link mitoribosome iron-sulfur cluster assembly to multiple mitochondrial dysfunctions syndrome. *Nucleic Acids Res.* **51**, 11797–11812 (2023).
55. L. Boß, O. Stehling, H.-P. Elsässer, R. Lill, Crucial role and conservation of the three [2Fe-2S] clusters in the human mitochondrial ribosome. *J. Biol. Chem.* **301**, 108087 (2025).
56. V. Schünemann, "From small molecules to complex systems: A survey of chemical and biological applications of the Mössbauer effect" in *Modern Mössbauer Spectroscopy*, Y. Yoshida, G. Langouche, Eds. (2021), pp. 173–219.
57. H. P. Gunnlaugsson, Spreadsheet based analysis of Mössbauer spectra. *Hyperfine Interact.* **237**, 79 (2016).
58. W. R. Hagen, Very low-frequency broadband electron paramagnetic resonance spectroscopy of metalloproteins. *J. Phys. Chem. A* **125**, 3208–3218 (2021).
59. D. Netz, Original_data_Duppe_et_al. Zenodo. https://zenodo.org/records/17488509. Deposited 30 October 2025.

Downloaded from https://www.pnas.org by Universitaetsbibliothek der RPTU Kaiserslautern-Landau on January 6, 2026 from IP address 131.246.60.80.

PNAS

Supporting Information for

The function of Mak16 in ribosome biogenesis depends on its [4Fe-4S] cluster

Nadine Duppe, Lukas Knauer, Marc Hagebölling, Lena Langner, Martin Stümpfig, Volker Schünemann, Antonio J. Pierik and Daili J. Netz

Antonio J. Pierik and Daili J. Netz
Emails: pierik@rptu.de and dnetz@rptu.de

This PDF file includes:

Supporting text
Figures S1 to S16
Tables S1 to S13
SI References

Supporting Information Text

Material and Methods

Yeast Strains. *Saccharomyces cerevisiae* W303-1A (MATa, *ura3-1*, *ade2-1*, *trp1-1*, *his3-11,15*, *leu2-3,112*) was used as wild-type strain. Exchange of the endogenous promoter of yeast genes by galactose regulatable promoters was achieved by homologous recombination. PCR-based DNA fragments designed according to (1) were amplified with the oligonucleotides listed in Table S5 and transformed using the lithium acetate method (2). In Gal-*MAK16* the promoter region of *MAK16* was replaced by the *natNT2* cassette from pYM-N27 (1). The same was done for the double mutant strains Gal-*MAK16*/Gal-*CFD1* and Gal-*MAK16*/Gal-*CIA1* which previously had their *CFD1* and *CIA1* promoter regions replaced by the *HisMX6* gene from pFA6a-HisMX6 (3). For the Gal-*MAK16*/Gal-*RPF1* strain the nucleotide-upstream promoter region of *RPF1* in Gal-*MAK16* was replaced by an adapted pYM-N27 template in which the *natNT2* gene was replaced by the *HisMX6* gene from pFA6a-HisMX6 (3). For the Gal-*MAK16*/Gal-*NBP35* strain the nucleotide-upstream promoter region of *NBP35* in Gal-*MAK16* was replaced by the *HisMX6* gene from pFA6a-HisMX6 (3). All constructs were verified by PCR amplification of chromosomal DNA, sequencing of the purified PCR fragments (see Table S6 for primers) and phenotypic analysis of yeast cells transformed with appropriate plasmids. The yeast strains used in this work are summarized in Table S7.

Cloning and Molecular Biology. For plasmids expressing yeast Mak16 or Rpf1 the coding sequence of *MAK16* and *RPF1* was amplified by PCR from genomic DNA of the W303-1A yeast strain. Templates for PCR amplification of *MAK16* from other organisms were a human *MAK16* cDNA clone (MGC:57551, Source Bioscience, UK) and genomic DNA from *E. cuniculi* and *T. brucei*, donated by Prof. J. Lukeš (University of South Bohemia, Czech Republic). The centromeric yeast vectors pRS414-*MET25* and pRS416-*MET25* (4) were used as “empty vectors” or recipient of DNA fragments, and named 414-*MET25* or 416-*MET25* for simplicity. In some yeast vectors the sequences coding for 3×HA (abbreviated HA) or 1×Myc (Myc) tags were introduced at the 5' end of *MAK16* and *RPF1*, respectively. The *E. coli* strains used are listed in Table S8. Primers used for plasmid construction are listed in Table S9. Cysteine to alanine variants were generated by amplification of plasmid templates with primer designed according to Zheng *et al*. (5) (Table S10), followed by *Dpn*I digestion to remove the parental template and transformation into *E. coli*. All yeast plasmids are listed in Table S11, and *E. coli* plasmids in Table S12. All constructs were verified by Sanger sequencing.

Growth Complementation Tests. For drop tests, exponentially growing cells were cultured in SC medium supplemented with 2 % (w/v) galactose or 2 % (w/v) glucose and diluted to an optical density (OD) at 600 nm of 0.1, followed by sequential 10-fold dilutions. Aliquots of 5 µL of undiluted and sequentially diluted cell suspensions were spotted onto solid SC agar media with the appropriate auxotrophy markers and sugar. Photographs were taken after 48 h of incubation at 30 °C. For the tests with redox stressors yeast cells were cultured for 16 hours in SC medium containing 2 % (w/v) glucose and auxotrophic markers, diluted to an OD_{600nm} of 0.2 and grown until the cells reached an $OD_{600\ nm}$ of 0.4, when they were treated with the redox stressing agents at the indicated concentration in the legend for 2 hours. The cells were then washed and spotted onto SC-glucose agar plates, as previously described or used for preparation of immunopulldowns at the indicated concentration of redox stressor.

^{55}Fe Incorporation. Yeast strains (see Table S7) were transformed with 416-*MET25* plasmids encoding HA-Mak16 from yeast or other organisms (see Table S10). To investigate the effect of depletion of key components of the ISC and CIA machineries, yeast cells transformed with 416-*MET25*-HA-Mak16 (from yeast) were grown in SC medium supplemented with 2 % (w/v) galactose or 2 % (w/v) glucose and auxotrophic markers for 24 h at 30 ˚C. Cells were then washed and incubated in iron poor SC medium supplemented with appropriate carbon source and auxotrophic markers for 16 h. Cells were again washed and resuspended in iron poor SC medium supplemented with appropriate sugar and auxotrophic markers, subsequently 10 µCi of $^{55}FeCl_3$ was added and cells were incubated for 2 h at 30 °C. To test whether Mak16 from other organisms is capable to bind ^{55}Fe expression was in W303-1A cells in 2 % (w/v) glucose supplemented SC medium. Protein extracts were prepared using normalized cell mass (0.5 g wet weight) in TNETG buffer (10 mM Tris/Cl pH 7.4, 2.5 mM EDTA, 150 mM NaCl, 10% (v/v) glycerol, 0.5% (v/v) Triton X-100) and 2 mM (end concentration) PMSF, using glass beads. An aliquot (25 µL) of the clarified supernatant was TCA-precipitated for further Western blot analysis (see below and Table S13 for antibodies). Mak16 was immunodetected using antibodies against the HA-tag (1:1000 diluted). Rabbit polyclonal antibodies were employed to document the depletion of ISC and CIA proteins. The remaining 200-250 µL were incubated with HA-agarose beads (HA-probe (F-7) AC sc-7392 AC, Santa Cruz Biotechnology) for 1 h at 4 ˚C. The immunoprecipitates were washed three times with TNETG buffer and resuspended in 50 µl of ddH_2O. After addition of 1 ml of scintillation

cocktail the ^{55}Fe radioactivity associated with the beads was measured by scintillation counting with settings appropriate for ^{3}H (6).

Western Blot Analysis. Samples for Western blot analysis were subjected to standard SDS-PAGE and subsequently transferred to nitrocellulose membranes (0.45 µm) using a Trans-Blot Turbo Transfer System® (Bio-Rad). The membrane was blocked with a BSA solution for monoclonal antibody detection and with skimmed milk for polyclonal antibody detection. Following the blocking step, the membrane was washed and then incubated with appropriate secondary antibody HRP conjugates, as detailed in Table S13. The membrane was then treated with enhanced chemiluminescence (ECL) reagent (BioRad), prepared by mixing the chemiluminescent substrate with 30% (w/v) hydrogen peroxide at a 1:1 ratio. Signal detection was performed using either the Fusion SL (Vilber Lourmat) or Chemostar (Intas) imaging system. In the Western blot images positive signals (luminescence) are displayed as dark bands on a white background from the signal inversion during image processing.

Protein-Protein Interaction: Co-immunoprecipitation was performed using wild-type or cysteine-to-alanine variants of yeast Mak16 and Rpf1, without any treatment or under conditions of redox stressors at specified concentrations. The experiments utilized affinity tags fused to Mak16 (N-terminal HA) and/or Rpf1 (N-terminal Myc). To avoid interference from endogenous, non-tagged copies, the Gal-Mak16/Gal-Rpf1 strain was employed. Following transformation with 416-*MET25*-HA-Mak16 (WT or variants) and 414-*MET25*-Myc-Rpf1 plasmids, yeast cells were cultured for 40 hours in SC medium supplemented with 2% (w/v) glucose and appropriate auxotrophic markers. The expression driven by the *MET25* promoter was reduced by adding 0.5 mM methionine (final concentration). Cell extracts were prepared from 0.5 g of yeast cells (wet weight) using glass beads in TNETG buffer, as previously described. An aliquot (50 µL) was precipitated with TCA for Western blot analysis, while 200–250 µL of the extract was incubated with either anti-HA-agarose beads (using either the HA-probe antibody (F-7, sc-7392, Santa Cruz Biotechnology, Fig. 5B) or magnetic anti-HA beads (Pierce #88830, Fig. 5D)) or Myc-agarose beads (using Myc antibody (9E10, sc-40, Santa Cruz Biotechnology, Fig. 5B) or magnetic anti-Myc beads (Pierce #88842, Fig. 5D)) for 1 hour at room temperature. The beads were then washed three times with TNETG buffer and resuspended in 50 µL Laemmli sample buffer (125 mM Tris-HCl, pH 6.8; 10% (v/v) glycerol; 2% (w/v) SDS; 0.1% (w/v) bromophenol blue; 100 mM DTT). Samples were subjected to SDS-PAGE and Western blotting. Anti-HA antibodies (diluted 1:2000 in Fig. 5B and 1:1000 in Fig. 5D) or anti-Myc antibodies (diluted 1:2000 in Fig. 5B and 1:1000 in Fig. 5D) were employed for detection. Chemiluminescence detection was performed as previously described.

Heterologous Protein Expression and Purification. Human and yeast Mak16 proteins were toxic when expressed in *E. coli* BL21 cells, a problem that was solved by the use of the more tightly controlled T7 Express LysY/Iq *E. coli* strain. Wild type and cysteine to alanine variants of yeast His_6-Mak16 were co-expressed with Rpf1 in pETDuet-1. After transformation three colonies were used for a 100 ml overnight preculture in LB medium plus ampicillin (0.1 µg/ml medium) at 30 °C. Of this preculture a 2 % inoculum was cultivated in the same medium until an $OD_{600\ nm}$ of 0.3 was reached. Then the temperature was decreased to 20 °C. Cells were induced with IPTG (0.5 mM, end concentration) at an $OD_{600\ nm}$ of 0.5 and further incubated for 16 h. Cells were harvested, transferred to a Coy anaerobic chamber and resuspended into lysis buffer (50 mM NaH_2PO_4, 300 mM NaCl, 10 mM imidazole, pH adjusted to 8.0 with NaOH). From this point onwards all steps were carried out anaerobically. Cell lysates obtained by sonication were centrifuged at 48,000 × g for 20 minutes. The resulting supernatant was applied to a 5 mL pre-packed Ni-NTA Agarose column (Cube Biotech), pre-equilibrated with lysis buffer, using an Äkta Start chromatography system (GE Healthcare) according to the manufacturer's instructions. The column was washed with lysis buffer containing 20 mM imidazole, and subsequently eluted with the same buffer containing 250 mM imidazole. When indicated, NaH_2PO_4 was replaced with 50 mM sodium pyrophosphate ($Na_4P_2O_7$). Immediately following elution, proteins were desalted using a PD-10 desalting column (GE Healthcare) pre-equilibrated with buffer containing 50 mM NaH_2PO_4 or $Na_4P_2O_7$ and 300 mM NaCl, adjusted to pH 9.0. Eluted proteins were either analyzed immediately or aliquoted, snap-frozen, and stored at –80 °C. If necessary, samples were concentrated using a 30-kDa cut-off centrifugal filter unit (Sartorius) prior to storage for later use. Western blotting followed by immunodetection with anti-His monoclonal antibodies was used to reveal which protein band on SDS-PAGE corresponded to the His-tagged Mak16 protein. Protein determination by the microbiuret/TCA method, and determination of non-heme iron and acid-labile sulfur were according to Pierik *et al.* (7). Extinction coefficients were calculated from the observed absorbance divided by the millimolar protein concentration, as determined by the microbiuret/TCA method.

EPR Analysis and EPR-mediated Redox Titrations. Purified Mak16, Mak16/Rpf1 or Mak16/Rpf1-Δ58 complex in desalting buffer (see previous section) were prepared for EPR analysis in the as isolated state, after oxidization with potassium ferricyanide (1 mM, final concentration) and after reduction with sodium dithionite (2 mM, final concentration) for 2-3 min in the Coy glove box. After transfer into EPR tubes and capping, the samples were subsequently frozen with liquid nitrogen outside the glove box. The determination of the redox potential of Mak16/Rpf1 in the presence or absence of ES7 was carried out in an anaerobic tent, using a mediator mixture containing 40 µM (final concentration) safranin O, neutral red, benzylviologen and methylviologen in 50 mM NaH_2PO_4 or $Na_4P_2O_7$ (as indicated in the legends) and 300 mM NaCl. The titration vessel was constantly stirred, during which a silver/silver chloride redox combination microelectrode (InLab™, Mettler Toledo, +207 mV vs. the hydrogen electrode) recorded the solution potential. After addition of small aliquots of 0.2-2 mM sodium dithionite in desalting buffer the potential was allowed to stabilize before samples were withdrawn for freezing and subsequent EPR analysis. EPR spectra were recorded with a Bruker Elexsys E580 X band spectrometer equipped with an Oxford Instruments ESR900 helium flow cryostat. A modulation amplitude of 1.5 mT and frequency of 100 kHz were used. Simulation of EPR spectra used the Gstrain5 program with LabVIEW as the graphical interface supplied by Prof. W.R. Hagen, TU Delft, the Netherlands (8). For spin integration 11.5 mM $CuSO_4$ in 10 mM HCl and 2 M $NaClO_4$ was used.

Mössbauer spectroscopy. ^{57}Fe metal powder was dissolved in 8 M HCl, followed by the addition of an equimolar amount of trisodium citrate dihydrate. The resulting solution was slowly neutralized to approximately pH 5 by addition of 12.5 % (w/v) aqueous ammonia. For ^{57}Fe incorporation, *E. coli* cells harbouring the appropriate plasmid were grown in LB medium supplemented with 50 µM ^{57}Fe-ammonium citrate (final concentration), inoculated with 1% (v/v) of an overnight preculture. Protein overexpression was performed as described in the section *Heterologous Protein Expression and Purification*. Eluted protein fractions in desalting buffer were concentrated to a final volume of ~400 µL using centrifugal spin concentrators. Samples were transferred to Mössbauer sample vials within an anaerobic chamber, if applicable reduced by addition of buffered sodium dithionite, rapidly frozen, and stored in liquid nitrogen. Mössbauer spectra were recorded in the constant acceleration mode with a conventional spectrometer from Wissel GmbH with a bath cryostat (Oxford Instruments, Abingdon, UK). Isomer shifts are given relative to α-Fe at 25 °C. Magnetically split spectra were simulated with the spin Hamiltonian formalism (9) with the program Vinda (10). Otherwise, spectra were analyzed by least squared fits using Lorentzian line shapes. For fitting of experimental Mössbauer spectra with more than two components the parameters for the species observed in isolation (oxidized human Mak16 for the 25 % component in dithionite reduced human Mak16 in the lower trace in Fig. 2B, and $[3Fe\text{-}4S]^{1+}$ from a difference spectrum at the bottom right for the other spectra in Fig. S15) were fixed.

RNA Isolation and Gel Electrophoresis. Total RNA was isolated from *Saccharomyces cerevisiae* strains W303-1A, Gal-*NFS1*, Gal-*NAR1*, and Gal-*CIA2* cultivated in synthetic complete (SC) medium supplemented with 2% (w/v) glucose or galactose, as indicated, and appropriate auxotrophic markers. RNA was also extracted from Gal-*MAK16* cells previously transformed with the empty vector 416-*MET25* or with 416-NP-Mak16 constructs encoding either wild-type or cysteine to alanine variants of Mak16. Single colonies were cultured for 24 h at 30 °C in the indicated carbon source, diluted into fresh medium to an initial $OD_{600\,nm}$ of 0.1 and then grown for approximately two doubling times. Cells were rapidly cooled on ice, washed with ice-cold RNase-free water, and harvested by centrifugation at 4 °C (corresponding to 4 $OD_{600\,nm}$ units, ~6.8×10^7 cells). Pellets were stored at −80 °C until RNA extraction. Total RNA was purified using the Monarch Total RNA Miniprep Kit (New England Biolabs) according to the manufacturer's instructions. RNA concentration and purity were determined using a NanoDrop spectrophotometer (Thermo Fisher Scientific). When indicated, RNA integrity and size distribution were analyzed by 1 % (w/v) agarose, 2.2 M formaldehyde gel electrophoresis using 30 mM tricine/30 mM triethanolamine buffer as running buffer. Samples were mixed with RNA loading buffer containing 0.025% (w/v) ethidium bromide. RiboRuler High Range RNA ladder (Thermo Fisher Scientific) was used as a molecular weight marker.

Northern Blot Analysis. Total RNA was extracted from *Saccharomyces cerevisiae* cells using the E.Z.N.A.® Yeast RNA Kit (Omega BioTek) following the manufacturer's instructions. RNA samples were resolved by electrophoresis on a 1 % (w/v) agarose gel containing 10 mM sodium acetate, 1 mM EDTA, 40 mM MOPS, pH 7.0 and 0.4 M formaldehyde. Following separation, RNA was transferred onto Hybond-N+ membranes (Amersham, GE Healthcare) using a TurboBlotter Downward Transfer System (Cytiva) with 10 × SSC (1.5 M NaCl and 0.15 M sodium citrate, pH 7.0) as the transfer buffer. RNA was crosslinked to the membrane using a BLX-254 UV crosslinker (Vilber Lourmat) at 245 nm for 1 min. Transfer efficiency was confirmed by ethidium bromide fluorescence present in the RNA loading buffer, visualized during the crosslinking step. Hybridization was performed with DIG-ddUTP-labeled probes specific to 18S (5′-CATGGCTTAATCTTTGAGACC-3′) and 25S (5′-CTCCGCTTATTGATATGC-3′)

rRNA. Probes were hybridized for 1 h at 37 °C (18S) and 45 °C (25S) in hybridization buffer containing 0.5 M sodium phosphate (pH 7.0), 7 % (w/v) SDS, and 1 mM EDTA. Membranes were washed sequentially in 2 × SSC with 0.1 % SDS for 5 min at room temperature and then for 5 min at 68 °C. For immunodetection, membranes were equilibrated in 0.15 M NaCl, 0.1 M maleic acid buffer (pH 7.5), then blocked for 30 min in the same buffer with 10 % (w/v) blocking reagent (Roche). Membranes were incubated with anti-digoxigenin-peroxidase (anti-DIG-POD) antibody (1:1000 dilution) in blocking solution for 1 h. After washing, chemiluminescent signals were developed using Clarity ECL substrate (Bio-Rad) and imaged with a Fusion SL documentation system (Vilber Lourmat). In the Northern blot images positive signals (luminescence) are displayed as dark bands on a white background from the signal inversion during image processing.

Synthesis of ES7-RNA. For the synthesis of ES7 RNA a DNA sequence was PCR amplified from yeast genomic DNA with a forward primer containing the minimal T7 promotor sequence (TAATACGACTCACTATAGGG) fused to the 5'-ES7 encoding DNA sequence (CATTTGATCAGACATG), and a reverse primer corresponding to the 3' end of ES7 (GGCATATAACCATTATGCCAGCATC). The amplified PCR product was used as template for the synthesis of ES7 using the HiScribe T7 Quick High Yield RNA synthesis kit (NEB). The run-off transcript started with the previously underlined GGG sequence. After digestion of the DNA template with DNase I, the synthesized ES7 RNA was isolated using the Monarch clean up kit with high capacity columns (NEB). ES7 RNA concentrations were quantified with a Nanodrop spectrophotometer (Fisher Scientific).

EMSA. To assess whether the synthesized ES7 could bind to the purified His_6Mak16/Rpf1-Δ58 complex, an electrophoretic mobility shift assay (EMSA) was conducted. A folding procedure was tested for the isolated ES7 RNA (see previous section) by incubation at 85°C for 30 seconds, followed by a cooling phase from 85 to 30 °C at a ramp rate of 1.5 °C/min in a buffer containing 50 mM sodium pyrophosphate, 300 mM NaCl, 1 mM DTT, 1 mM $MgCl_2$, and 10 % (v/v) glycerol (binding buffer). As the mobility of the RNA on non-denaturing gels did not change, this procedure was omitted in later experiments. Mixtures of purified His_6Mak16/Rpf1-Δ58 complex and ES7 RNA were loaded onto a 5 % (w/v) native acrylamide gel and electrophoresed in 45 mM Tris, 45 mM boric acid, 1 mM EDTA buffer. RNA was visualized after a 30-minute incubation with GelRed (1:10000 dilution), followed by washing and detection using an imaging system (Chemostar, Intas or Fusion SL, Vilber Lourmat). The gel was subsequently stained with Coomassie Brilliant Blue to visualize proteins.

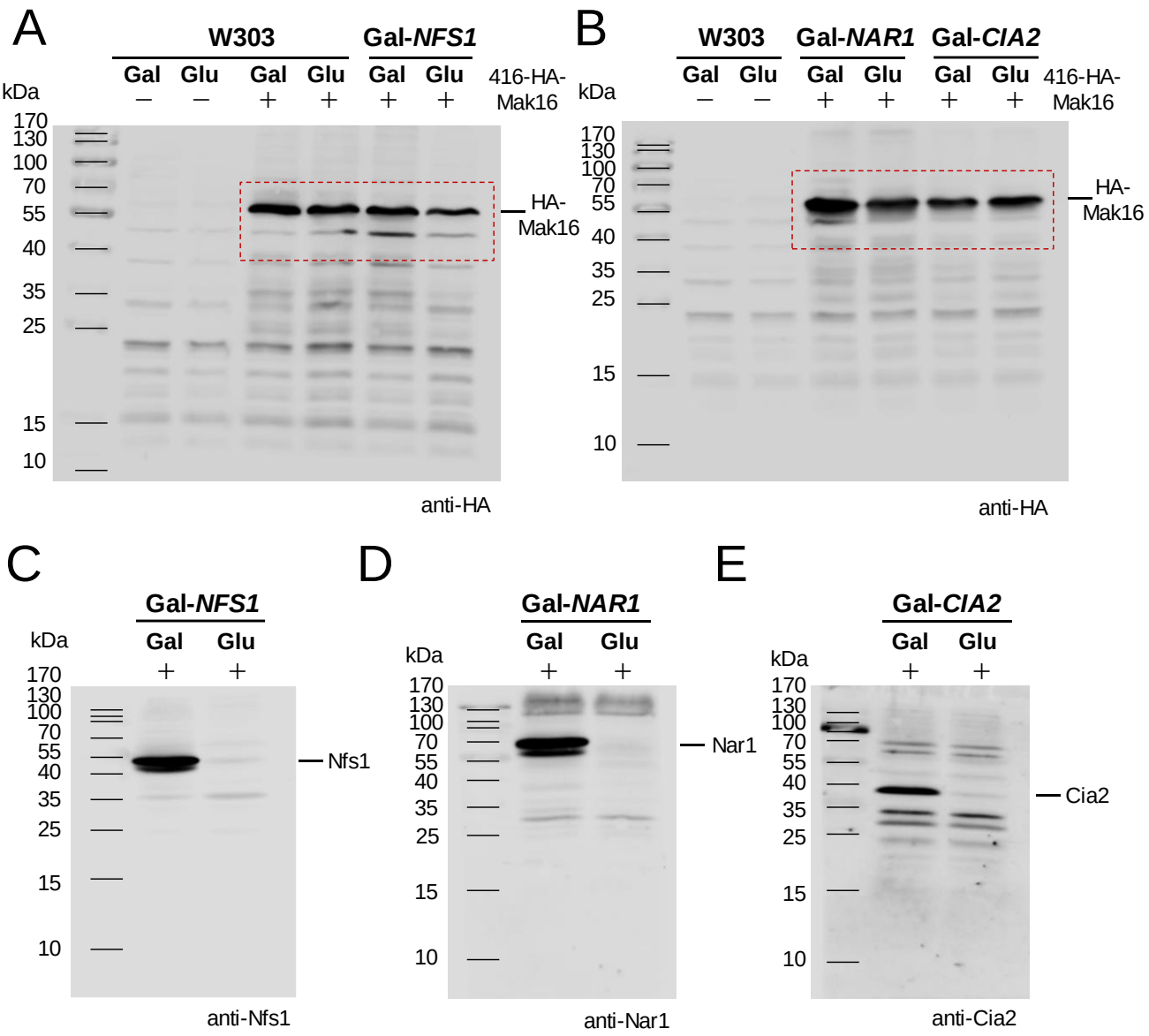


Fig. S1. Non-cropped images of Western blots shown in **Fig. 1A-B**. Red boxes depict the area of the images in the main text. Yeast wild type (W303) and the Gal-*NFS1* (**A**), Gal-*NAR1* and Gal-*CIA2* (**B**) strains transformed with 416-*MET25*-HA-Mak16 were grown under permissive (galactose, Gal) and non-permissive (glucose, Glu) conditions for 40 h in SC medium supplemented with the appropriate sugar. Cell extracts were prepared, subjected to SDS-PAGE and Western blotting. Commercial murine monoclonal antibodies against HA were used at a dilution of 1:1000, anti-mouse secondary antibodies at dilution of 1:10000. The efficiency of depletion of Nfs1 (**C**), Nar1 (**D**) and Cia2 (**E**) was assessed by Western blot analysis of the cell extracts as in (**A**) and (**B**) employing polyclonal antibodies raised against each protein in rabbits at a dilution of 1:1000 and anti-rabbit secondary antibodies at dilution of 1:10000.

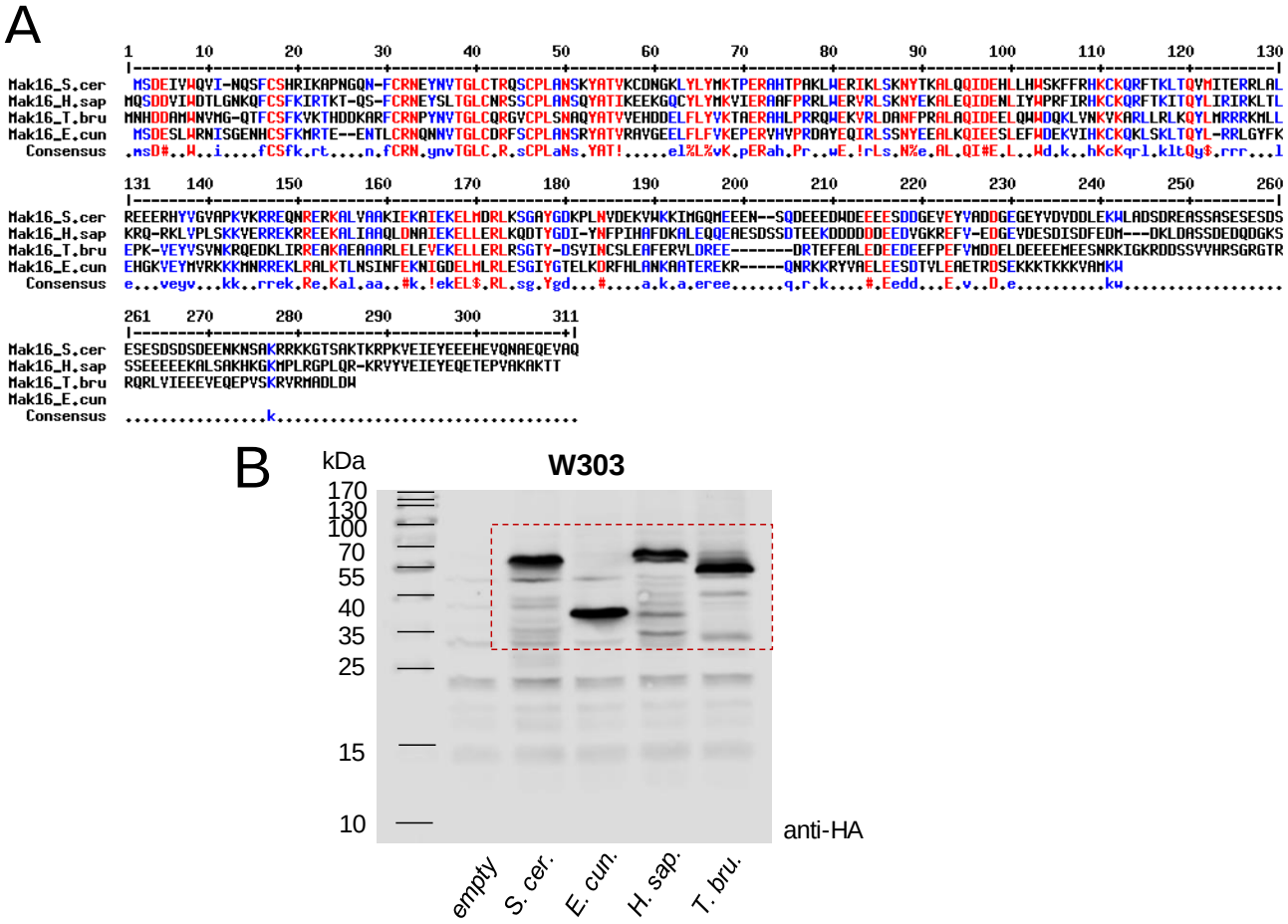


Fig. S2. (**A**) Amino acid sequence alignment (MultAlin (11)) between the sequences of Mak16 from *Saccharomyces cerevisiae*, *Homo sapiens*, *Trypanosoma brucei* and *Encephalitozoon cuniculi*, from top to bottom. (**B**) W303 yeast cells transformed with 416-*MET*25-HA-Mak16 from indicated eukaryotes were grown in glucose containing SC medium for 40 h, cell extracts were subjected to SDS-PAGE and Western blotting. Murine monoclonal antibodies against HA were used at a dilution of 1:1000, anti-mouse secondary antibodies at dilution of 1:10000. (**C**) Mak16 function in yeast cannot be substituted by tested homologues. The Gal-*MAK16* strain was transformed with 416 plasmids, containing yeast Mak16 or its homologues under the control of either the yeast *MAK16* promoter (NP) or the *MET25* promoter, as indicated. Cells were cultured in SC media containing galactose or glucose for 40 h, serially diluted 10-fold starting from an $OD_{600\ nm}$ of 0.5, and spotted onto plates. Growth was monitored for 2–3 days, with photographs taken at the end of the incubation period.

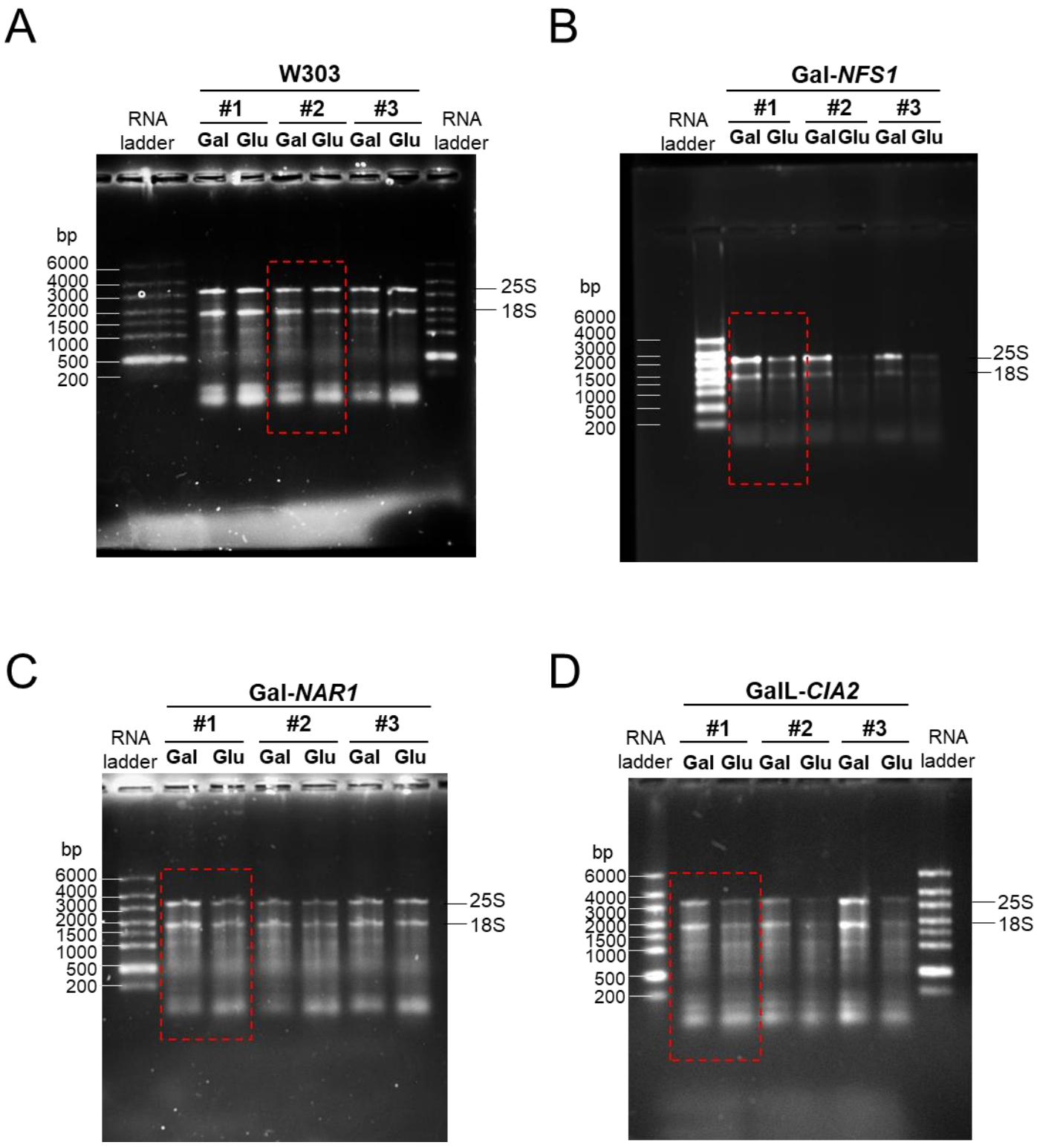


Fig. S3. (A-D) Non-cropped agarose gel electrophoresis showing total RNA extracted from the indicated yeast strains grown on galactose (Gal) or glucose (Glu), corresponding to the data in **Fig. 1D.** Data for three experiments (#1, #2 and #3) are shown. Gels were post-stained with GelRed and documented using ChemoStar Touch (Intas).

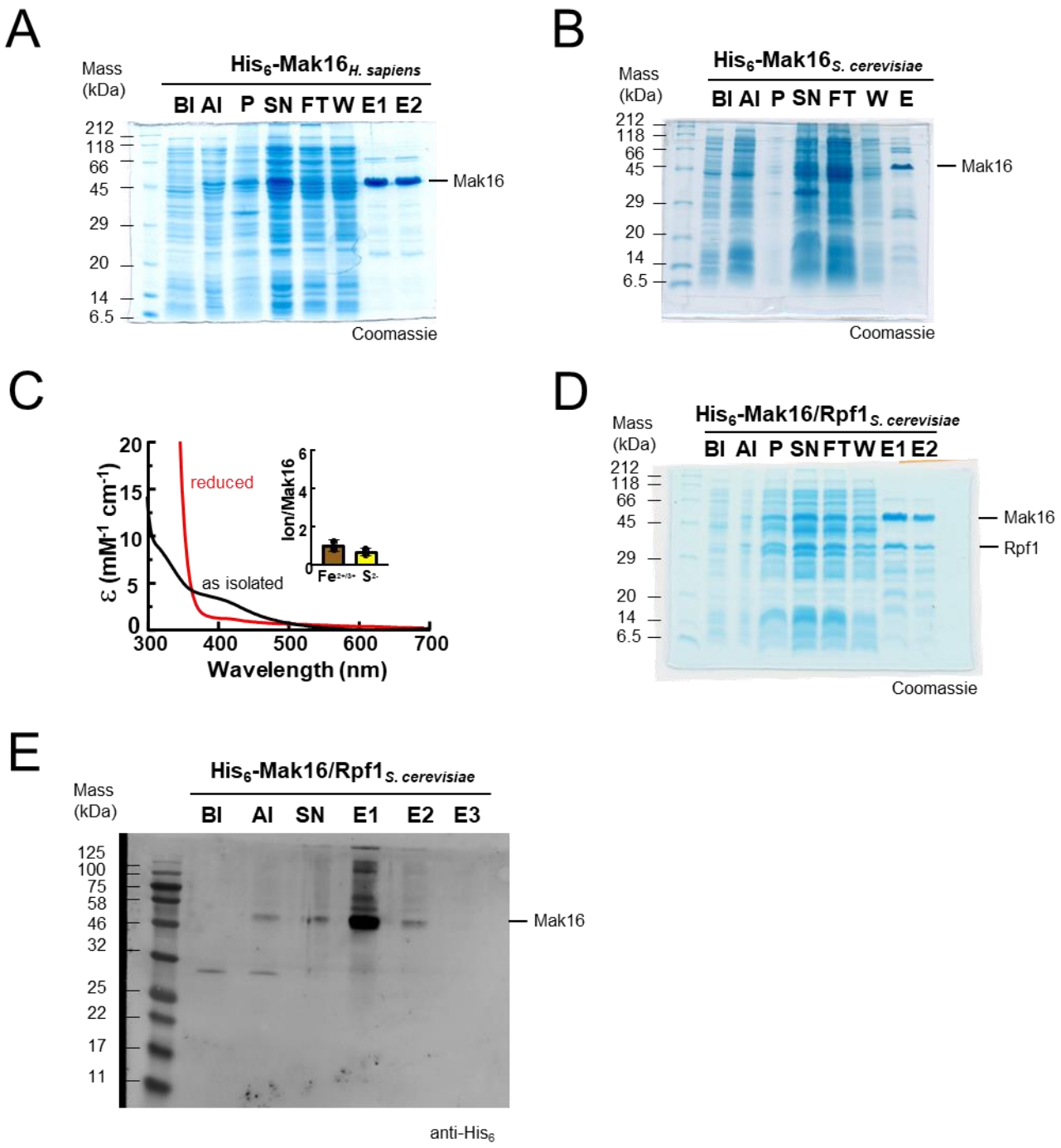


Fig. S4. (**A**) SDS-PAGE demonstrating the production and isolation of human His_6-Mak16 (data corresponding to **Fig. 2A**). (**B**) SDS-PAGE illustrating the expression and purification of yeast His_6-Mak16. (**C**) UV-Vis spectra of yeast His_6-Mak16 in its as isolated form (black line) and dithionite reduced form (red line), along with quantification of non-heme iron and acid-labile sulfide (inset). (**D**) SDS-PAGE for co-expression of yeast His_6-Mak16 with yeast Rpf1. (**E**) Western blot of co-expressed yeast His_6-Mak16/Rpf1, probed with a rabbit anti-His polyclonal antibody (1:1000 dilution) and anti-rabbit secondary antibodies at dilution of 1:10,000.

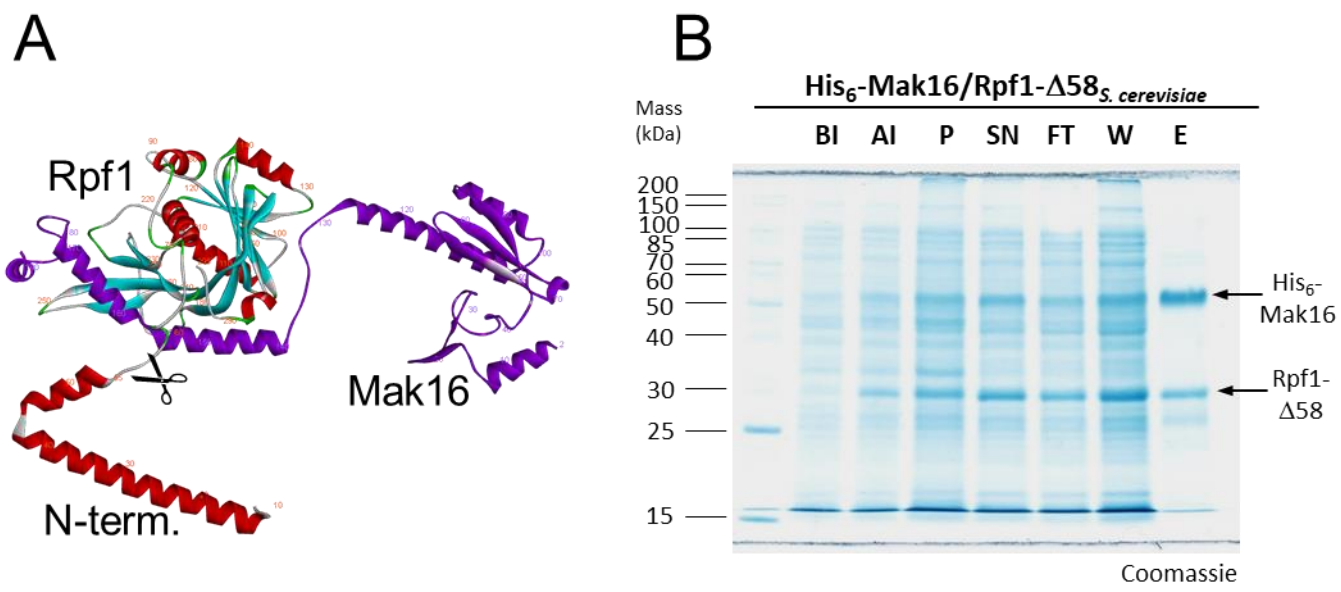


Fig. S5. (**A**) Visualization of the yeast Mak16-Rpf1 module (PDB ID: 6C0F). The truncation site, for removal of the N-terminal 58 amino acids of Rpf1 is marked with a scissors icon. The visualization, including the depiction of structural components, was created using BIOVIA Discovery Studio 2024. (**B**) SDS-PAGE analysis showing the overexpression and purification of yeast His_6-Mak16 co-expressed with Rpf1 truncated at its N-terminus to position 58.

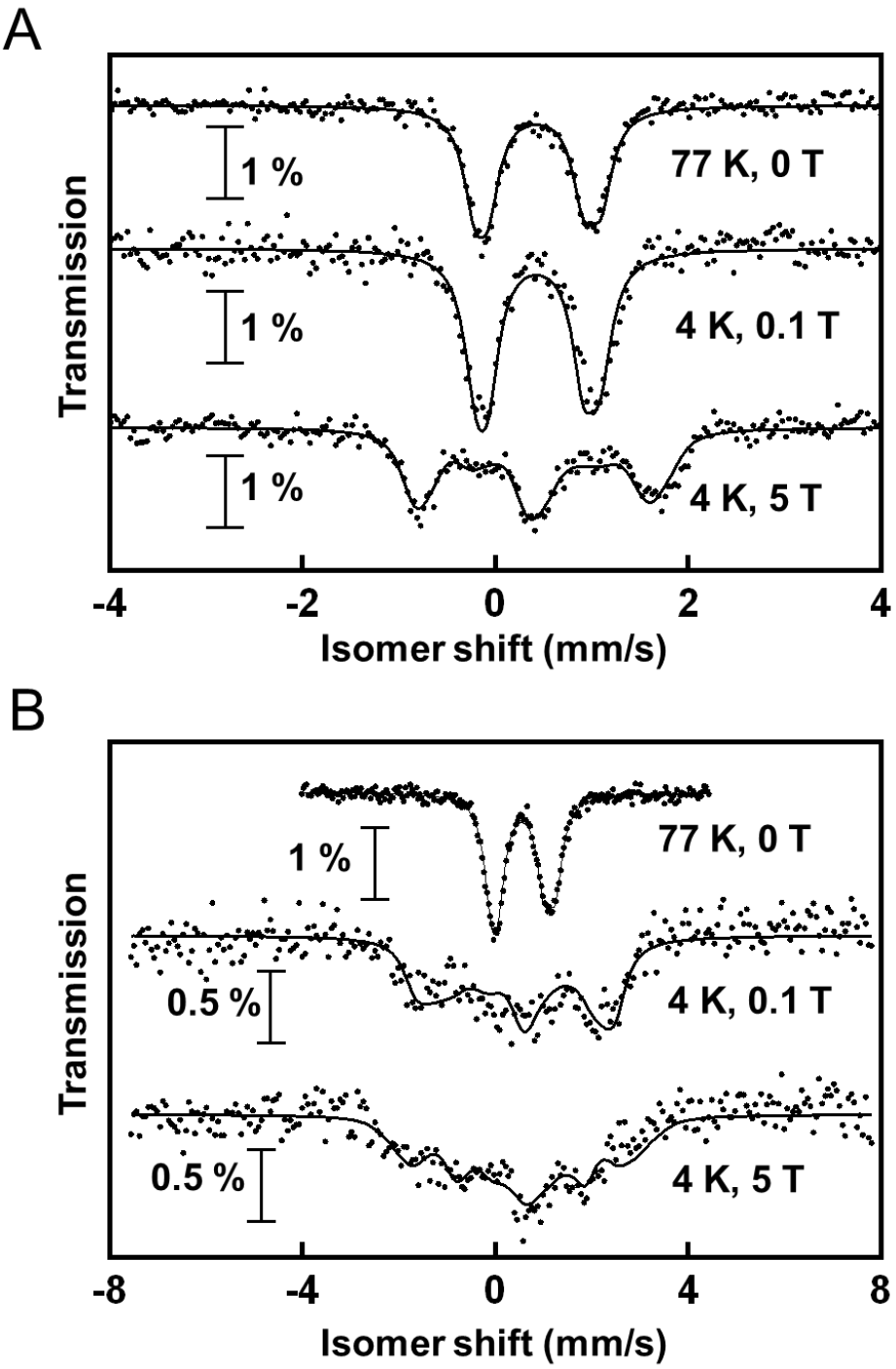


Fig. S6. Mössbauer spectra of the anaerobically purified yeast His-Mak16/Rpf1-Δ58 complex in 50 mM sodium phosphate buffer, 300 mM NaCl, pH 8.0 (**A**) and after incubation with sodium dithionite (4 mM, final concentration) for 2 min. (**B**). For Mössbauer parameters see Table S1. The top traces in both panels are identical to the experimental spectrum with the fit to the experimental data (solid trace) at 77 K as shown in the main text, **Fig. 2 F**, as the top and bottom trace, respectively. The middle and lower trace is for the same sample recorded at 4 K at an applied magnetic field parallel to the γ rays of 0.1 T and 5 T, respectively. In (**B**) spectra were recorded at a broader range of velocities to reveal splitting due to the paramagnetism of the *S*=1/2 cluster. The solid traces are fits based on Mössbauer parameters for the $[4Fe\text{-}4S]^{1+}$ cluster of *Bacillus stearothermophilus* ferredoxin (Table 2 in (12)).

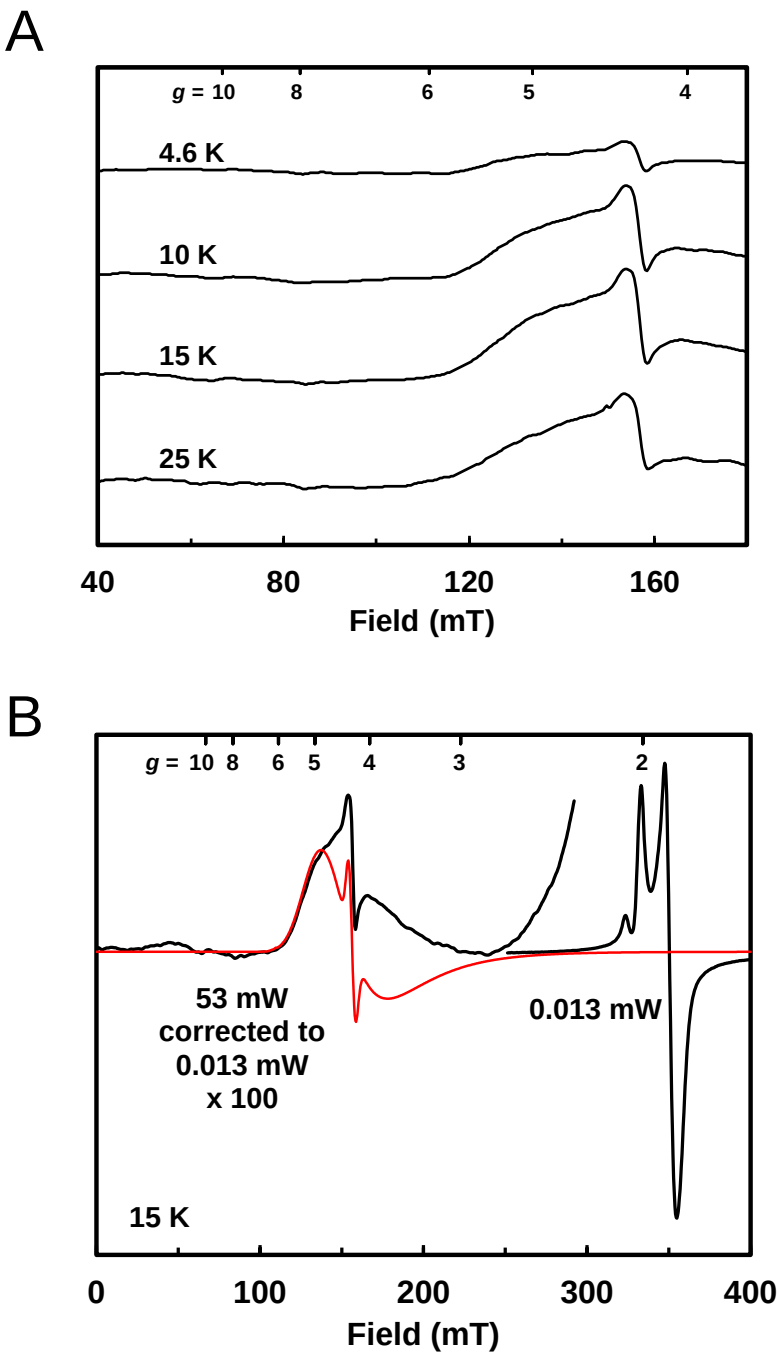


Fig. S7. EPR spectra of purified yeast His-Mak16/Rpf1-Δ58 complex in 50 mM sodium phosphate buffer, 300 mM NaCl, pH 9.0 after incubation with sodium dithionite (4 mM, final concentration) for 2 min. (**A**) Temperature dependence of the high spin spectral features. The intensities were corrected for a Curie law dependence, i.e. the *g*=4.4 signal is from an excited state. EPR conditions: microwave power, 50 mW, modulation amplitude, 1.5 mT, microwave frequency, 9.352 GHz. (**B**) Simulation (red) assuming that signal derives from the |±½⟩ doublet as excited state of a *S*=3/2 system with parameters as in Table S3. The low field region was recorded under conditions as in (**A**), but the intensity was divided by 64 (to correct the amplitude to a microwave power of 0.013 mW) and amplified 100-fold. The *g*=2 region was recorded at a microwave power of 0.013 mW.

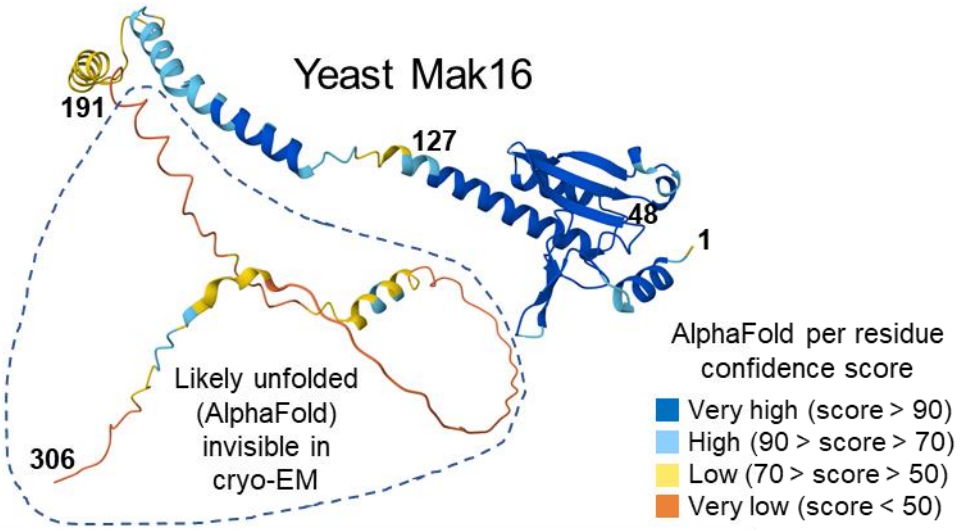


Fig. S8. AlphaFold model of yeast Mak16 with labelled positions of domains. Position 1-191 has defined electron density in the cryo-EM structure, position 192-306 is not visible.

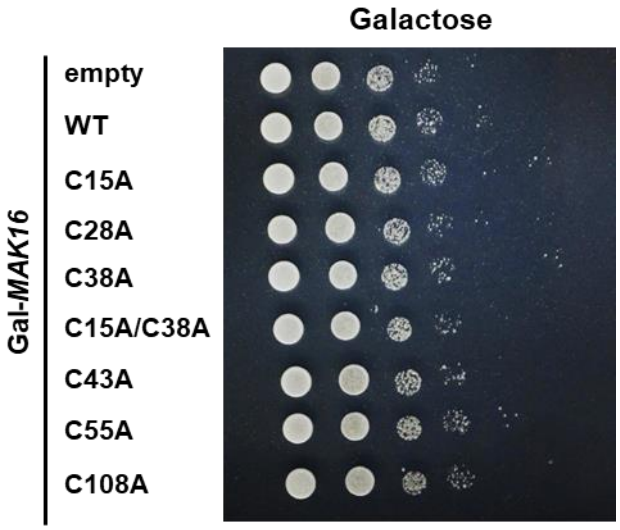


Fig. S9. Drop tests for Gal-*MAK16* yeast cells, transformed with 416 plasmids under control of the *MAK16* promoter under permissive conditions. Cells transformed with a plasmid lacking an insert (empty), or encoding wild type (WT) or indicated cysteine variants of Mak16, were cultured for 16 h in galactose containing SC medium. OD-normalized 10-fold serial dilutions were spotted on agar plates of the same medium and photographed after 2 days at 30 °C.

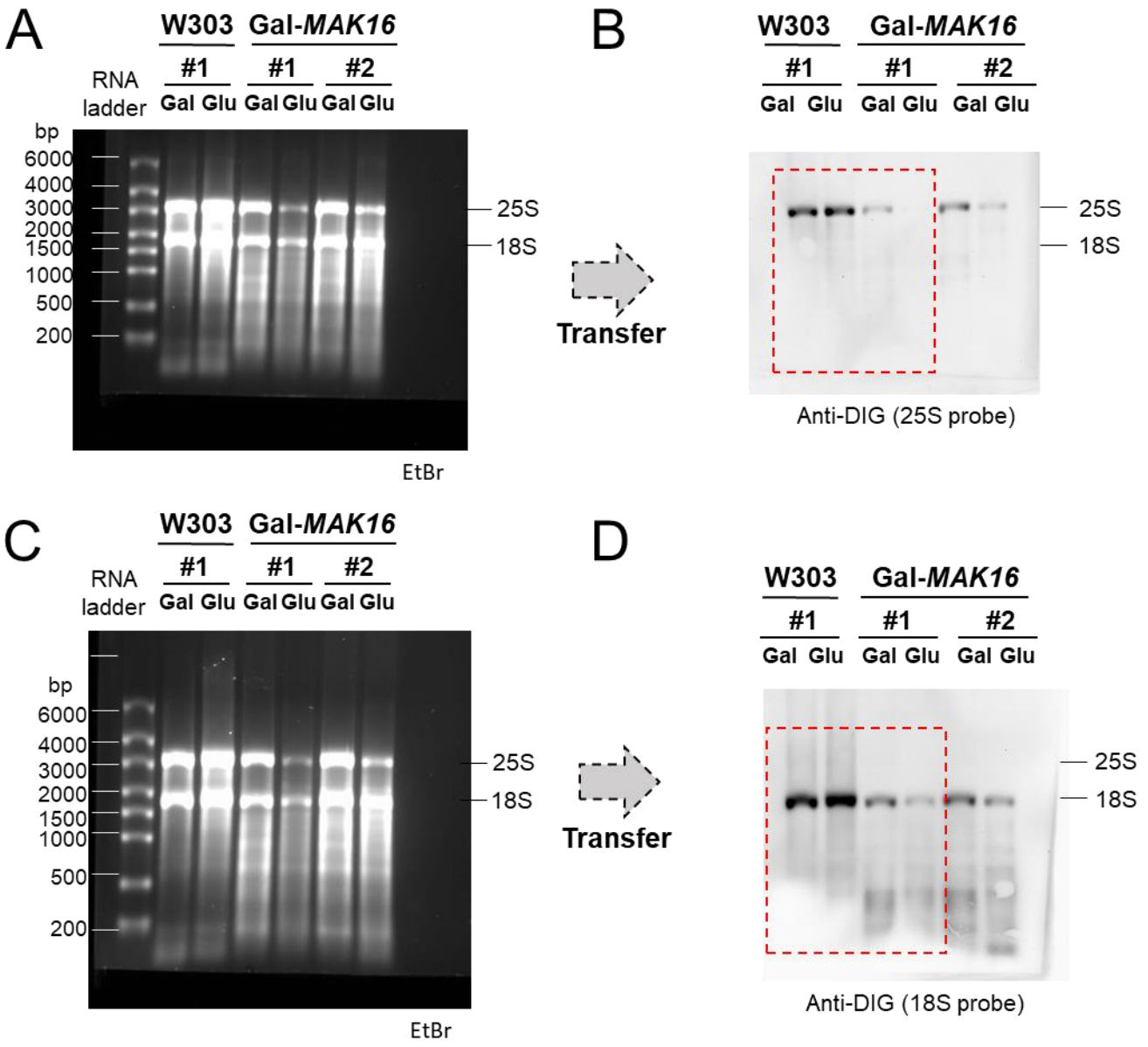


Fig. S10. Ethidium bromide visualization of total RNA isolated from wild type (W303) and Gal-*MAK16* yeast cells cultivated for 40 h in SC medium containing galactose (Gal) or glucose (Glu) subjected to agarose electrophoresis. After documentation by transillumination ((**A**) and (**C**)), RNA was transferred to a nylon membrane. In these Northern blots 25S or 18S rRNA was visualized with digoxigenin-ddUTP labelled probes and anti-digoxigenin-peroxidase conjugate ((**B**) and (**D**)). Marked areas correspond to the data shown in **Fig. 3C**.

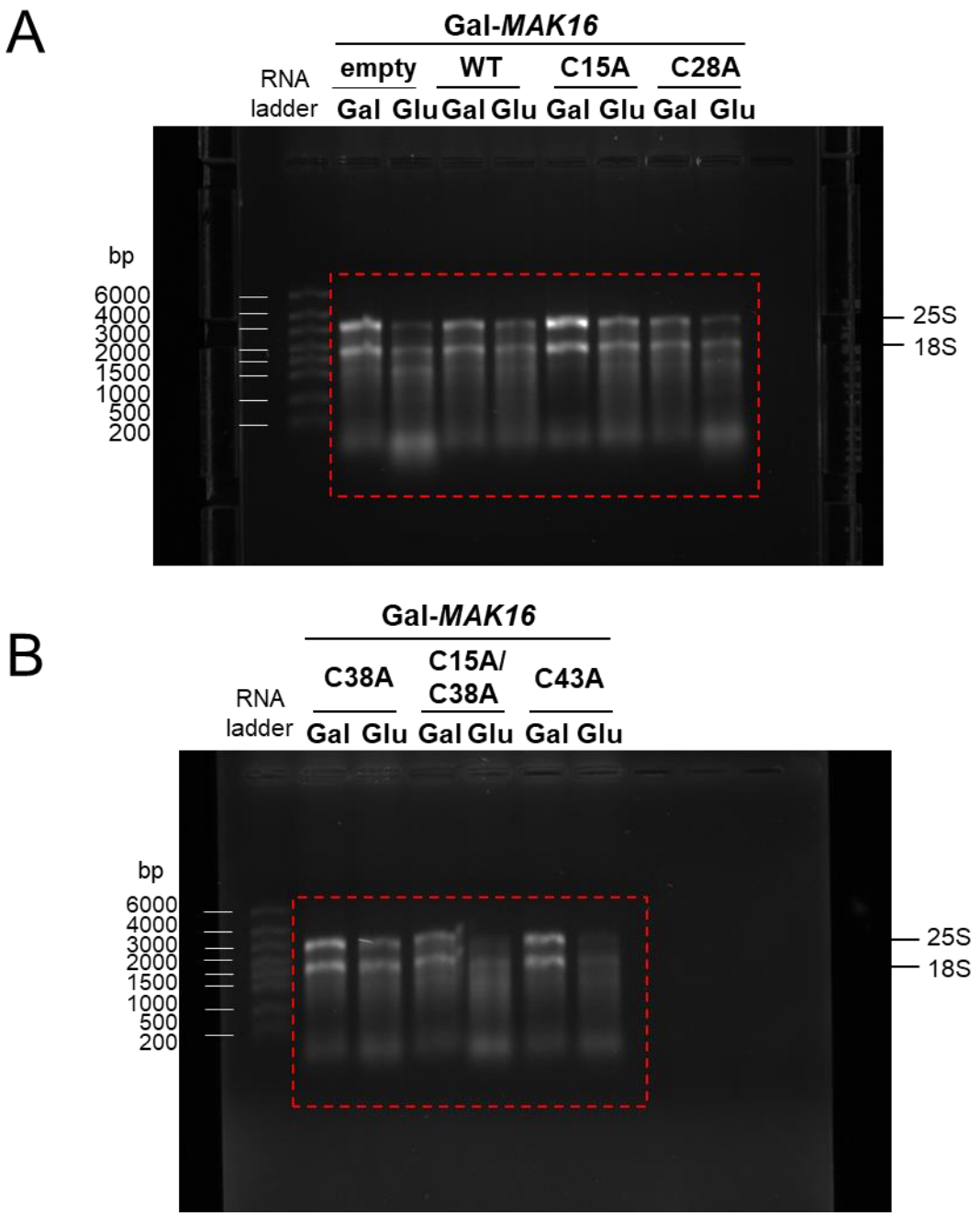


Fig. S11. (A-B) Uncropped agarose electrophoresis gels showing total RNA extracted from Gal-*MAK16* yeast cells transformed with empty vector, or 416NP vectors encoding wild-type and cysteine variants of Mak16. Growth was in galactose (Gal) or glucose (Glu) containing SC media. Gels were post-stained with ethidium bromide and documented using ChemoStar Touch (Intas). Marked areas correspond to the cropped data in **Fig. 3E**.

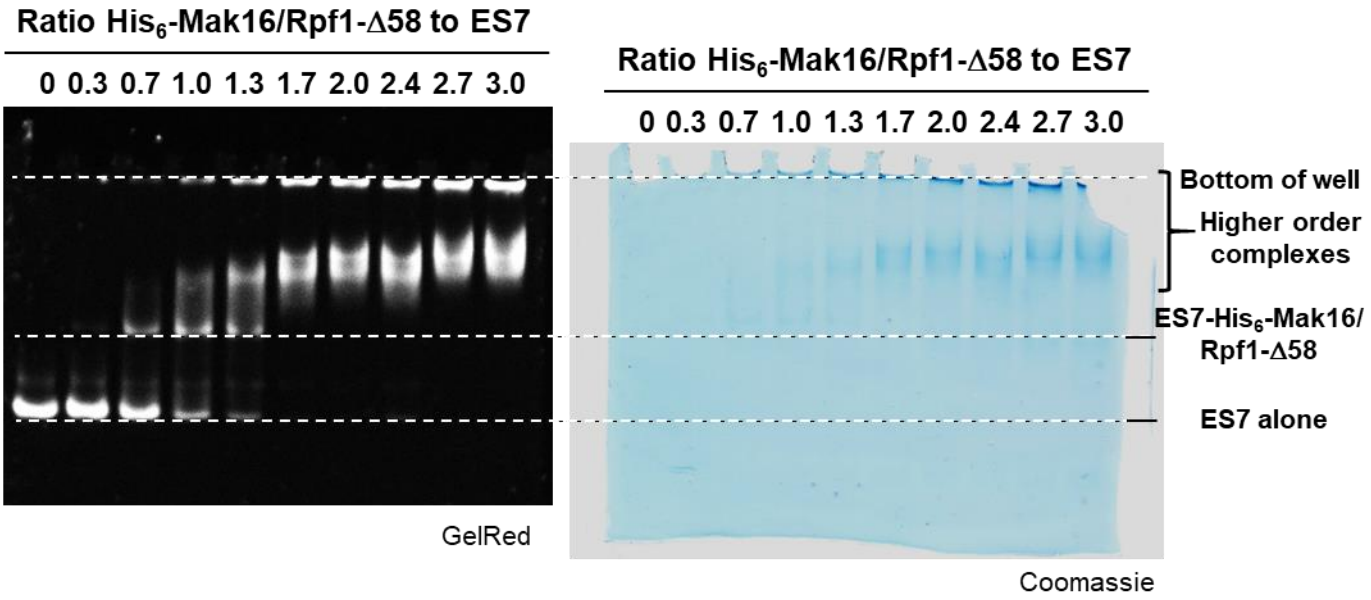
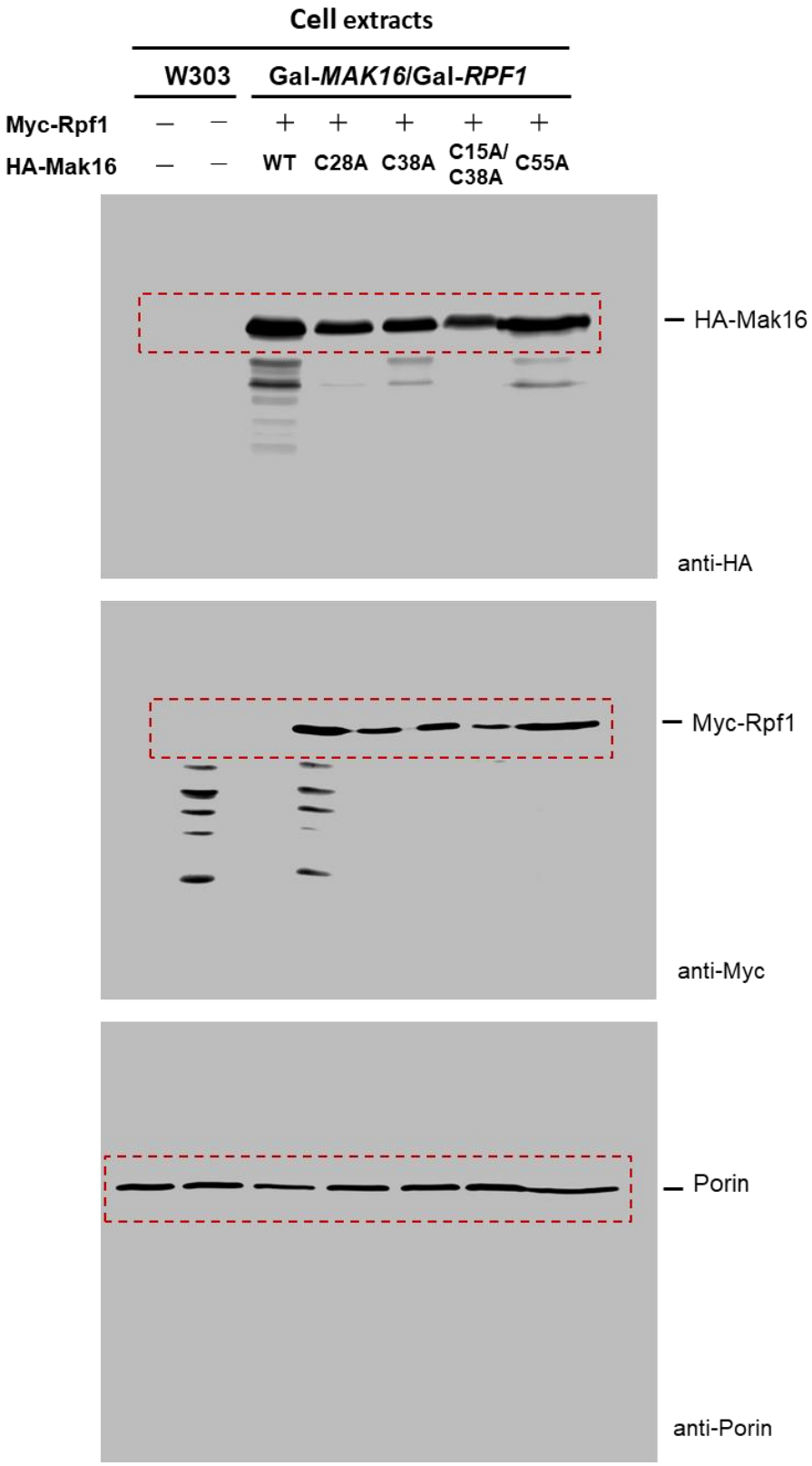


Fig. S12. Coomassie stained gel (right) after 5 % non-denaturing acrylamide gel electrophoresis and ChemoStar Touch (Intas) documentation of RNA with GelRed (left, **Fig. 4C).** The photograph and gel documentation are aligned to show which RNA bands correspond to RNA-Mak16//Rpf1-Δ58 complexes at different His_6Mak16/Rpf1-Δ58 to rRNA (ES7) ratios.


Cell extracts
W303
Gal-MAK16/Gal-RPF1
Myc-Rpf1
HA-Mak16
WT
C28A
C38A
C15A/ C38A
C55A
HA-Mak16
anti-HA
Myc-Rpf1
anti-Myc
Porin
anti-Porin

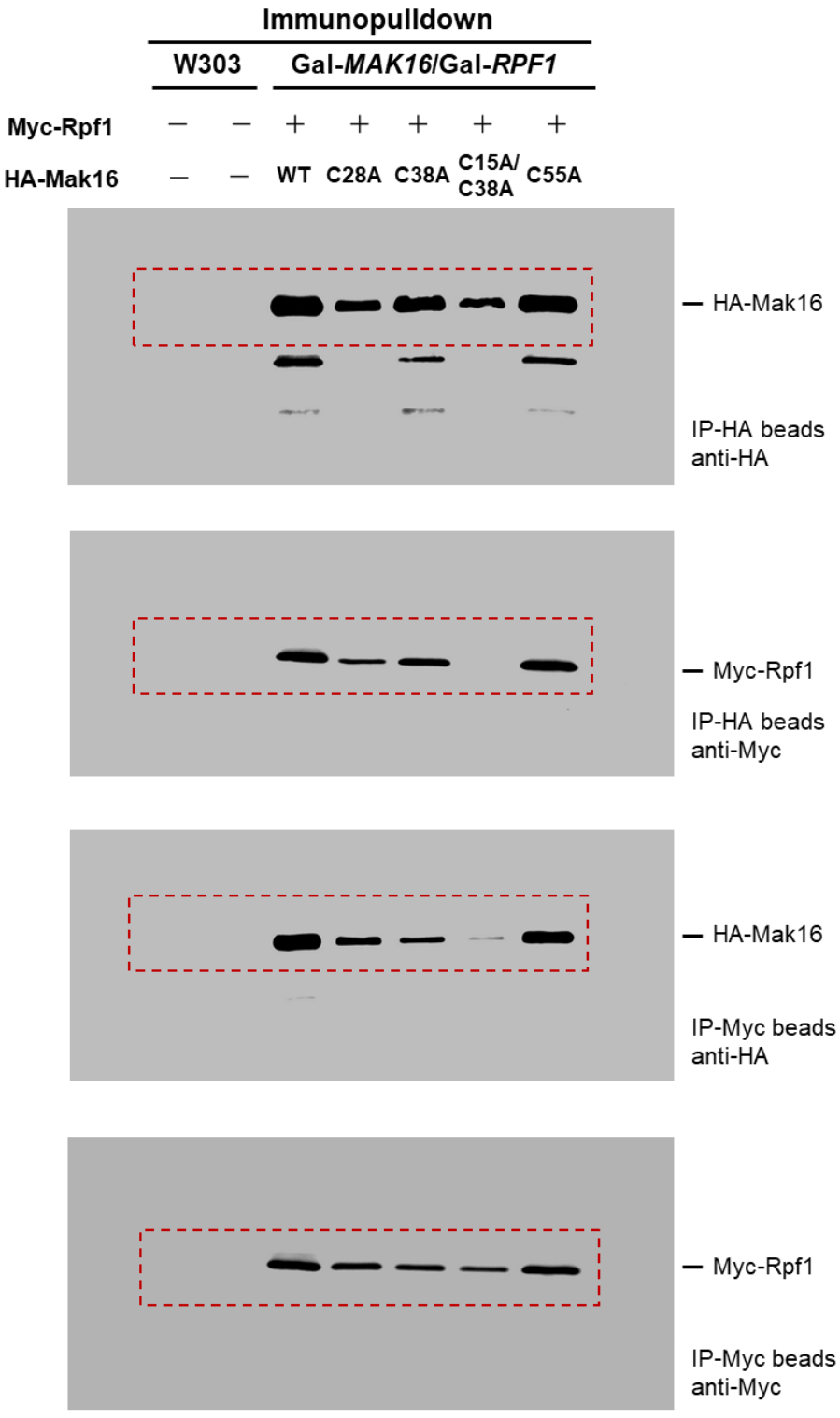


Fig. S13. Non-cropped images of Western blots shown in **Fig. 5B**. Red boxes mark the areas of the images in the main data. Polyclonal rabbit antibodies raised against porin (dilution 1:1000), primary monoclonal antibodies against HA and Myc tags were used at a dilution of 1:2000 and secondary anti-rabbit IgG antibodies at dilution 1:10,000.

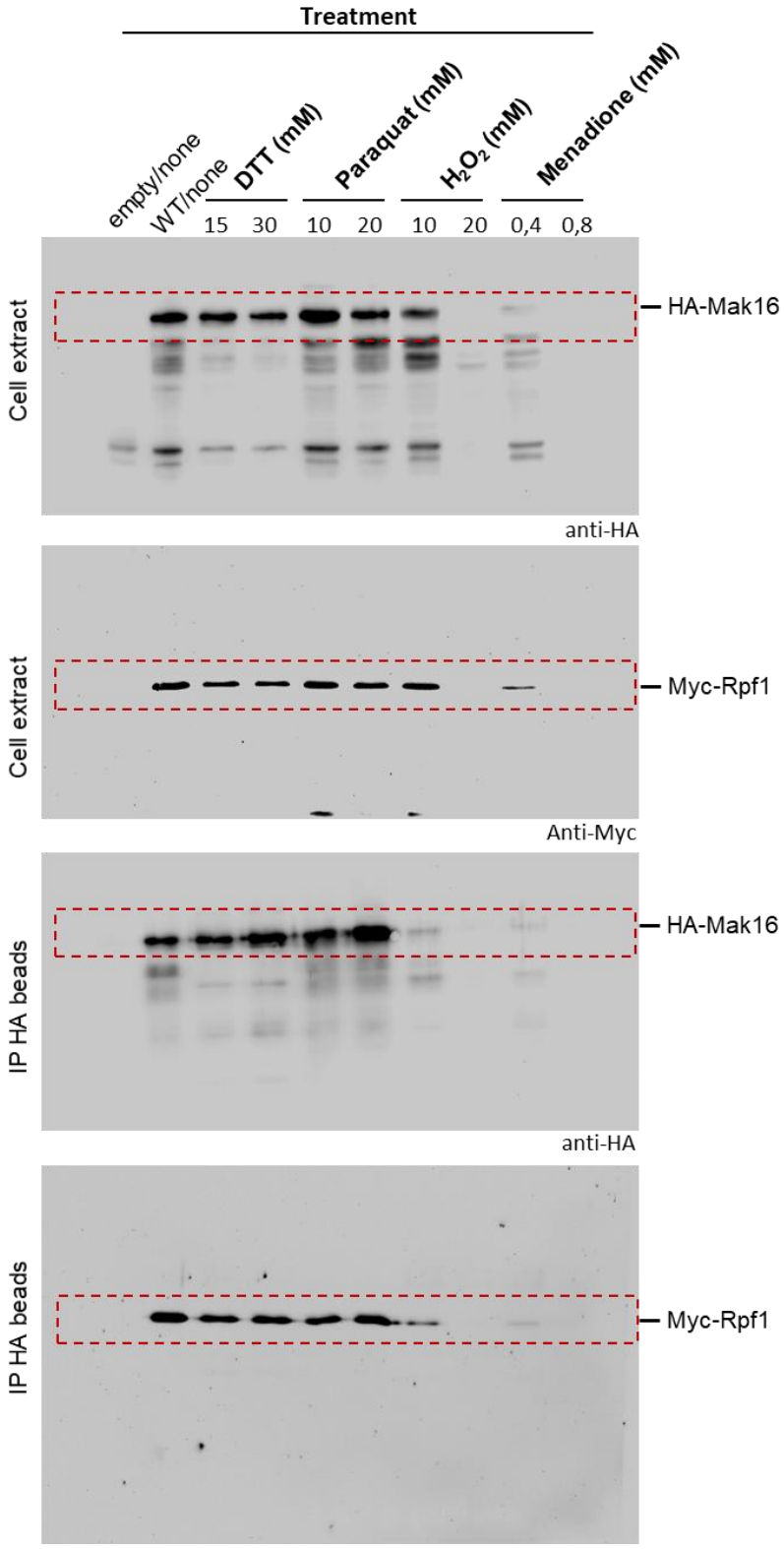


Fig. S14. Non-cropped images of Western blots shown in **Fig. 5D**. Red boxes mark the areas of the images in the main data. Monoclonal antibodies against HA and Myc tags were used at a dilution of 1:1000; anti-rabbit secondary antibodies were used at 1:10,000 dilution.

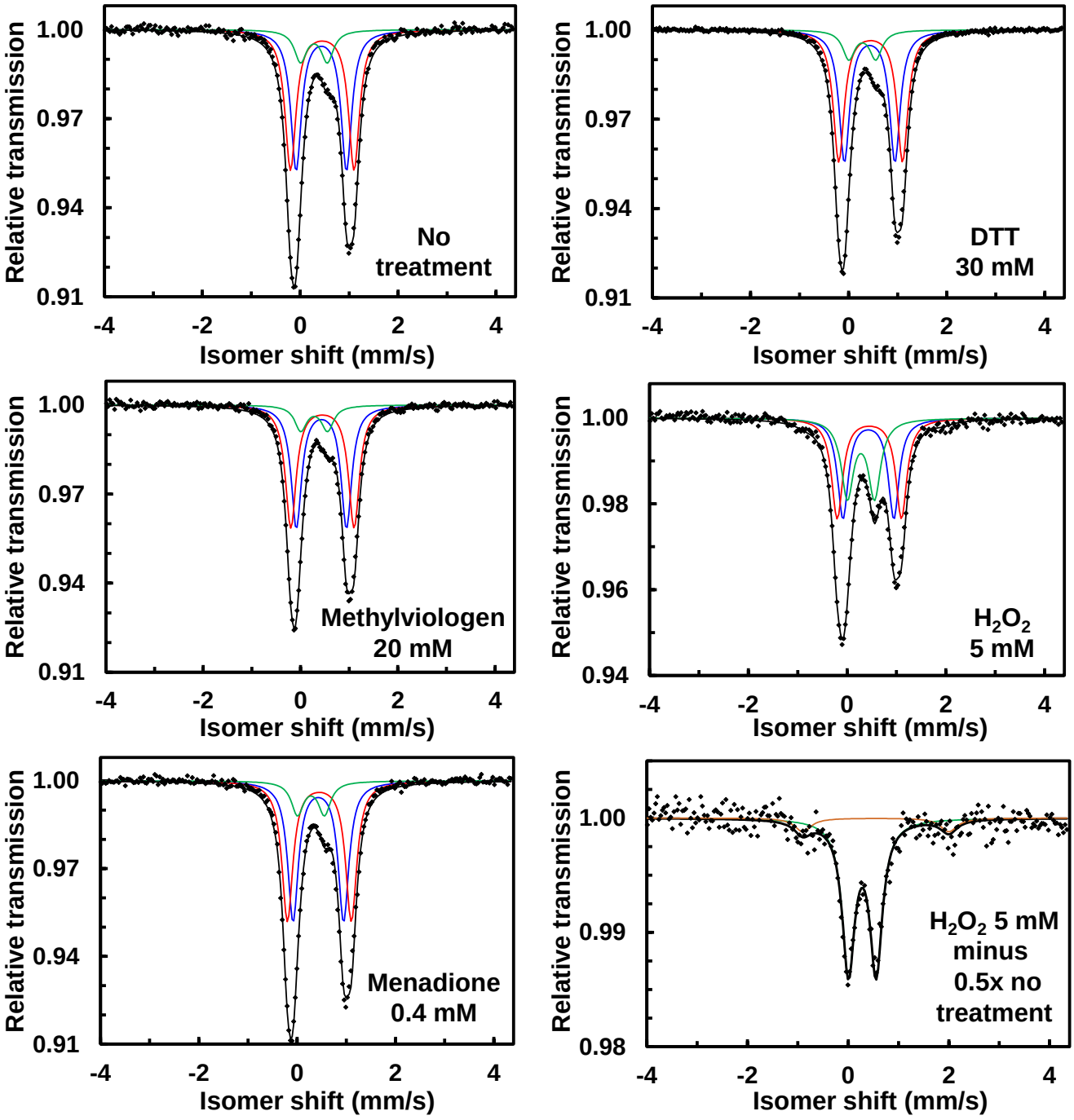


Fig. S15. Mössbauer spectra recorded at 77 K of ^{57}Fe enriched purified yeast His-Mak16/Rpf1-Δ58 complex in 50 mM sodium phosphate buffer, 300 mM NaCl, pH 9.0 after treatment with indicated components for 30 min. at 23 °C. Simulations are for the $[4Fe\text{-}4S]^{2+}$ quadrupole doublets (red and blue) and a quadrupole doublet for $[3Fe\text{-}4S]^{1+}$ (green). Mössbauer parameters in Table S1. The lower intensity of the sample treated with 5 mM H_2O_2 was due to non-optimal positioning of the sample in the cryostat. At the bottom right the difference spectrum for the determination of the Mössbauer parameters for the $[3Fe\text{-}4S]^{1+}$ and a minor ferrous component (brown) is shown.

A

C-terminus of Mak16	Organism
EEEVEQEPVSKRVRTADLDW	*Trypanosoma brucei brucei* TREU927
EEEVEHEHAPKRMRTADLDW	*Trypanosoma congolense* IL3000
IEEEVEHEQQKRSRLDDLDW	*Trypanosoma cruzi strain* CL Brener
EEEVEREQGTKRARLDDMEW	*Trypanosoma vivax* Y486
EEVERELPPRQRSRLEDLEW	*Leishmania braziliensis* MHOM/BR/75/M2904
EEVEQELAPRQRARLEDLEW	*Leishmania tarentolae*
EEVERELAPRQRARLEDLEW	*Leishmania major strain* Friedlin
DTTKSRKKSKSKKKSKQLEW	*Enterocytozoon bieneusi* H348
EAETRDSEKKKTKKKVAMKW	*Encephalitozoon cuniculi* GB-M1
ESCGVEKKADKKTKKTAMKW	*Encephalitozoon intestinalis* ATCC 50506
YEKEEEFYPLDRTHKISWDW	*Theileria annulata*
IEEEIENEPLKRVRQEDLDW	*Angomonas deanei*
LEEEVEREPRQRLRPEDIEW	*Leptomonas pyrrhocoris*
IEEEVEHEAPKRARREELDW	*Strigomonas culicis*
LEEEVEREPLQRARPEDLDW	*Crithidia fasciculata*
EREVEYDSKAKKTQRDELDW	*Bodo saltans*
PYVEIEYEQEQETANGDLNW	*Phytophthora infestans* T30-4
HIEYEQERENEKIPAVQHSW	*Schizosaccharomyces pombe*
SVEVEYEEDNGEKEKQMVDW	*Yarrowia lipolytica* CLIB122

B

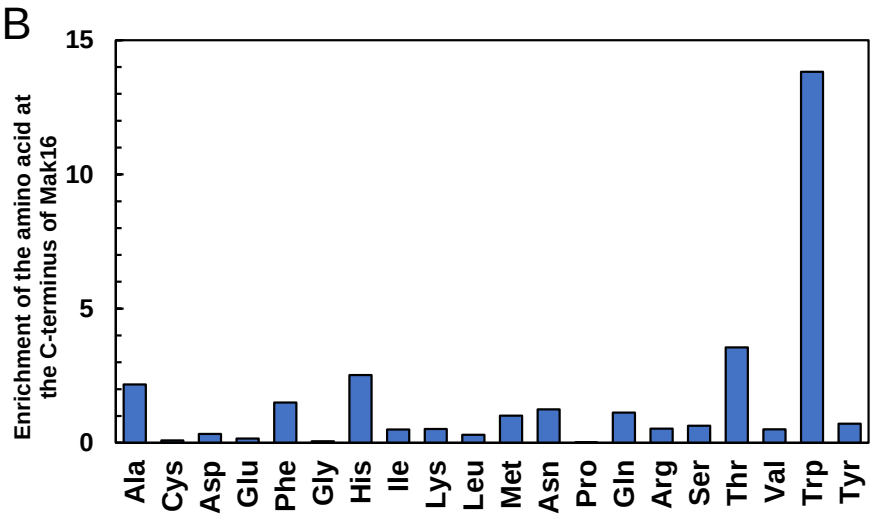


Fig. S16. (A) Tryptophan occurs at the C-terminus of Mak16 in eukaryotes, especially in many trypanosomal and microsporidial species. **(B)** Enrichment of tryptophan at the C-terminus in a collection of 1900 eukaryotic full-length Mak16 proteins. The percentage of the individual amino acids was divided by the average content in the entire human proteome.

Table S1. Parameters for the fits of the Mössbauer spectra of human and yeast Mak16.

Sample	Temp. (K)	δ (mm/s)[a]	ΔE_Q (mm/s)[a]	Γ (mm/s)[a]	η	Occup. (%)[a]
$[4Fe\text{-}4S]^{2+}$ as isolated Mak16 *Homo sapiens*	77	0.42	0.99	0.31		50
		0.44	1.31	0.31		50
$[4Fe\text{-}4S]^{1+}$ dithionite treated Mak16 *Homo sapiens* (75 % red.)[b]	77	0.54	0.90	0.38		37.5
		0.61	1.52	0.51		37.5
$[4Fe\text{-}4S]^{2+}$ as isolated Mak16/Rpf1-Δ58 *Saccharomyces cerevisiae*[c]	77	0.43	1.03	0.26		50
		0.45	1.30	0.27		50
$[3Fe\text{-}4S]^{1+}$ as isolated Mak16/ Rpf1-Δ58 *Saccharomyces cerevisiae*[c]	77	0.28	0.55	0.30		15
Fe^{2+} 5 mM H_2O_2 treated Mak16/ Rpf1-Δ58 *Saccharomyces cerevisiae*[c]	77	0.55	2.90	0.40		5
$[4Fe\text{-}4S]^{2+}$ as isolated Mak16/Rpf1-Δ58 *Saccharomyces cerevisiae*	4	0.42	0.99	0.28	0	50
		0.44	1.29	0.29	0	50
$[4Fe\text{-}4S]^{1+}$ dithionite treated Mak16/ Rpf1-Δ58 *Saccharomyces cerevisiae* (100% red.)	77	0.53	0.96	0.36		50
		0.58	1.33	0.36		50
$[4Fe\text{-}4S]^{1+}$ dithionite treated Mak16/ Rpf1-Δ58 *Saccharomyces cerevisiae* (100% red.)[d]	4	0.52	1.05	0.52	0.5	50
		0.58	1.27	0.52	0.5	50

[a] Experimental errors for the Mössbauer parameters are $\pm$ 0.02 mm/s. Occupancies have an accuracy of $\pm$ 3 %.

[b] Parameters for the oxidized form were kept fixed and were taken from the fit for the as isolated state (but with 12.5 and 12.5 % occupancy).

[c] The simulations of the two quadrupole doublets of the $[4Fe\text{-}4S]^{2+}$ cluster were based on the more concentrated non-treated sample in Fig. S15 (top left). However, the latter sample had a clear $[3Fe\text{-}4S]^{1+}$ component, contrary to the sample shown in Fig. 2F, which had < 5% of this component. The parameters for the $[3Fe\text{-}4S]^{1+}$ component were determined by fitting the Mössbauer difference spectrum of 5 mM H_2O_2 treated minus non treated. Just detectable ferrous ions were simulated with the parameters in this table.

[d] The spectra at 4 K were too noisy to determine the $A/g_N\beta_N$ tensors from the experiment. Therefore the values for the *Bacillus stearothermophilus* ferredoxin were used (12). Parameters for the $A/g_N\beta_N$ tensor were -23, -24 and -19 T for the $Fe^{2.5+}$-$Fe^{2.5+}$ doublet, and 20, 10 and 10 T for the Fe^{2+}-Fe^{2+} doublet. The underlined values were slightly adapted.

Table S2. Mössbauer parameters for $[4Fe\text{-}4S]^{2+}$ containing proteins.

Protein	Organism	Temp. (K)	δ (mm/s) $Fe^{2.5+}$	ΔE_Q (mm/s) $Fe^{2.5+}$	Occup. (%)	Ref.
HiPIP	*Allochromatium vinosum*	77	0.42	1.12	100	(13)
HiPIP	*Allochromatium vinosum*	77	0.42	1.13	100	(14)
Ferredoxin	*Bacillus stearothermophilus*	77	0.42	0.98	100	(15)
Ferredoxin[a]	*Bacillus stearothermophilus*	77	0.43	1.36	25[a]	(12)
			0.43	1.07	25[a]	
			0.43	0.86	25[a]	
			0.42	0.57	25[a]	
GPAT	*Bacillus subtilis*	100	0.43	1.17	100	(16)
Nitrogenase Fe protein	*Azotobacter vinelandii*	80	0.43	1.14	75	(17)
			0.425	0.77	25	
Photosystem I Fx	*Synechococcus sp*. PCC 6301	80	0.43	1.06	100	(18)
APS reductase[a]	*Desulfovibrio gigas*	100	0.42	1.28	25[a]	(19)
			0.43	1.11	25[a]	
			0.43	0.88	25[a]	
			0.41	0.55	25[a]	
Enoate reductase	*Clostridium tyrobutyricum*	130	0.43	1.315	100	(20)
Iron-sulfur flavoprotein	*Methanosarcina thermophila*	100	0.45	1.12	100	(21)
HypD	*Escherichia coli*	77	0.43	0.95	100	(22)
PsaC ferredoxin	*Synechococcus sp*. PCC 7002	80	0.44	1.07	100	(23)
ABCE1	*Sulfolobus solfataricus*	77	0.43	1.32	50	(24)
			0.42	0.86	50	
NreB	*Staphylococcus aureus*	80	0.44	1.16	100	(25)
Benzoyl-coenzyme A epoxidase	*Azoarcus evansii*	80	0.44	1.10	100	(26)
Cfd1/Nbp35	*Saccharomyces cerevisiae*	80	0.43	1.18	100	(27)
Benzylsuccinate synthase	*Thauera aromatica*	80	0.43	1.09	100	(28)
PhrB	*Agrobacterium tumefaciens*	80	0.42	1.26	100	(29)
Dre2	*Saccharomyces cerevisiae*	80	0.43	0.99	50	(30)
			0.43	1.29	50	
Mak16	*Homo sapiens*	77	0.42	0.99	50	
			0.44	1.31	50	
Mak16	*Saccharomyces cerevisiae*	77	0.43	1.03	50	
			0.45	1.30	50	

[a] The Mössbauer spectra were fitted with four quadrupole doublets, though theory clearly defines two Fe^{2+}-Fe^{3+} ($Fe^{2.5+}$) pairs, which should yield two doublets. For **Fig. 2C** in the main text the average of the isomer shifts and quadrupole splittings of the two doublets with the lowest and highest quadrupole splittings was used.

Table S3. EPR simulation parameters for Fig. 2D and S7B.

Protein	Weight	$g_{av.}$	g_z	g_y	g_x	w_{zz}	w_{yy}	w_{xx}	w_{yz}	w_{xz}	w_{xy}
Human	0.50	1.933	2.001	1.918	1.880	0.020	0.010	0.045	0.000	0.000	0.000
Mak16	0.30	1.931	2.010	1.905	1.878	0.009	0.010	0.017	0.000	0.000	0.000
(reduced)	0.20	1.952	2.055	1.910	1.890	0.025	0.010	0.032	0.000	0.000	0.000
Yeast Mak16 (oxidized)	1.00	2.001	2.026	2.008	1.968	0.006	0.010	0.027	0.000	0.004	0.010
Yeast Mak16	0.69	1.936	2.015	1.909	1.885	0.013	0.013	0.033	0.000	0.000	0.005
(reduced)	0.29	1.947	2.071	1.890	1.880	0.016	0.015	0.030	0.000	0.000	0.000
$S = 3/2$	0.02	3.40	4.50	3.33	1.90	0.5	1.0	2.8	0.000	0.000	0.000
$S = 5/2$	0.0002	4.28	4.28	4.28	4.28	0.07	0.07	0.07	0.000	0.000	0.000

Table S4. Mössbauer parameters for [4Fe-4S]$^{1+}$ containing proteins.

Protein	Organism	Temp. (K)	δ (mm/s) $Fe^{2.5+}$	ΔE_Q (mm/s) $Fe^{2.5+}$	δ (mm/s) Fe^{2+}	ΔE_Q (mm/s) Fe^{2+}	Ref.
Ferredoxin	*Bacillus stearothermophilus*	77	0.50	1.18	0.60	1.82	(15)
Ferredoxin	*Bacillus stearothermophilus*	77	0.49	1.20	0.59	1.84	(12)
Ferredoxin	*Desulfovibrio gigas*	90	0.51	1.07	0.60	1.67	(31)
Nitrogenase Fe protein HMPA	*Azotobacter vinelandii*	50	0.53	0.94	0.58	1.51	(17)
Nitrogenase Fe protein ethyleneglycol	*Azotobacter vinelandii*	50	0.53	0.98	0.59	1.60	(17)
APS reductase cluster I	*Desulfovibrio gigas*	70	0.51	1.26	0.60	2.00	(19)
APS reductase cluster II	*Desulfovibrio gigas*	100	0.50	0.85	0.57	1.35	(19)
Enoate reductase	*Clostridium tyrobutyricum*	100	0.50	1.22	0.61	2.32	(20)
Iron-sulfur flavoprotein	*Methanosarcina thermophila*	100	0.50	0.90	0.57	1.68	(21)
Mak16	*Homo sapiens*	77	0.54	0.90	0.61	1.52	
Mak16	*Saccharomyces cerevisiae*	77	0.53	0.96	0.58	1.33	
Ferredoxin	*Clostridium pasteurianum*	77	0.57	1.25	0.57[a]	1.25[a]	(32)
GPAT	*Bacillus subtilis*	100	0.56	1.05	0.56[a]	1.05[a]	(16)
Nitrogenase Fe protein urea	*Azotobacter vinelandii*	50	0.54	0.80	0.54[a]	1.20[a,b]	(17)
Photosystem I Fx	*Synechococcus sp.* 6301	80	0.55	1.21	0.55[a]	1.21[a]	(18)
Activator HgdC	*Acidaminococcus fermentans*	80	0.53	0.95	0.53[a]	0.95[a]	(33)
PsaC ferredoxin	*Synechococcus sp.* PCC 7002	80	0.53	1.13	0.53[a]	1.13[a]	(23)

[a] The Mössbauer spectra were fitted with a single quadrupole doublet with parameters, which appear to be in between Mössbauer parameters for the Fe^{2+}-Fe^{3+} ($Fe^{2.5+}$) and Fe^{2+}-Fe^{2+} pairs.
[b] As in [a], but with two doublets with different linewidths.

Table S5. Primers for the construction of yeast strains.

Name	Sequence (5‘ → 3‘)	Strain
Mak16_S1	GTG ATT GGT ATA GAG GCA GAT ATT GCA TTG CTT AGT TCT TTC TTT TGA TGC GTA CGC TGC AGG TCG AC	Gal-*MAK16*
Mak16_S4	CTA TGA GAG CAG AAA CTT TGA TTA ATC ACT TGC CAA ACA ATT TCG TCG GAC ATC GAT GAA TTC TCT GTC G	
Mak16_For	GAT TCC CTC GCT AGA CAG G	
Mak16_Rev	GTG CTA CAC CAA CGT AGT GTC	
Gal1_prom_Nbp35	CGC ATT CAT TAA TGG TGT AAT TAG TAA TGC GTA GAA ATA TTT TGA TCG ATG AAT TCG AGC TC	Gal-*NBP35*
Gal1_orf_Nbp35	CTG CTG GTA GCA CTT CGT CGT TTA CAT GTG GTA GTA TCT CAG TCA TCG AAT TCC TTG AAT TTT C	
Check_Nbp35_For	CAC AAT TCT CTC AGT TCT ATG C	
Check_Nbp35_Rev	AAG TGC CCA ACT TAG CAT TGC	
GalL_prom_Cia2	AGT CGA ATA TAA AAT CTT GCT ACT GCA TTA TTC TAC GAT TTC CTG TTA TCG TAC GCT GCA GGT CGA C	Gal-*CIA2*
GalL_orf_Cia2	AGT TGG TTC TCC TCT AAA ATG TCG GGA TTT TCA TTC AAA AAC TCA GAC ATC GAT GAA TTC TCT GTC G	
Check_Cia2_For	CGC AAT GCT TGG GTG TAC GG	
Check_Cia2_Rev	GAC TTA ACG GGT GCT CAG GG	
Cfd1_prom_control	CAC ATC GAT AAG AGT GAA ACA TAT CC	Gal-*MAK16*/ Gal-*CFD1*
Cfd1_354-Rev	CAT AGA AGT CTT CTT AGG ACC C	
GalCia1_Nterm	CAT ATC TTT TCC TTG TAA AGT TTC AAA GAC TTA ATC AGA TTG ATA GAC GCC ATC GAA TTC CTT GAA TTT TC	Gal-*MAK16*/ Gal-*CIA1*
PromCia1_control	GCA CTT CTA- TCT TGT TTT GTG TTG C	
GalL_Rpf1_S1	CGA TTG AAC ACCT AA GGA AGA GGT AAA GCA GGC TTA ATA TAT TGA AAT ACG TAC GCT GCA GGT CGA C	Gal-*MAK16*/ Gal-*RPF1*
GalL_Rpf1_S4	TCT TGC CTC TTT AGC TTG TTT GTG ATG TTT ATC TCA TTA CCG AGA GCC ATC GAT GAA TTC TCT GTC G	
Rpf1_331-Rev	CAA ATT CAT AAG CGC TCT TCT TAG CG	
Rpf1_–169-For	TCA GTG CAT TTT TCA TTT TCG CGT TCG	

Table S6. Sequencing primers.

Name	Sequence (5‘ → 3‘)
Seq1_Mak16	GAT TCC CTC GCT AGA CAG G
Seq2_Mak16	GTC CGA CGA AAT TGT TTG GC
Seq3_Mak16_Rev	GGT TGT TAT TAT GGT ACA GTG CG
Cia1_Seq1	GAA GCG CTT CGG AAT TCA G
Cia1_Seq2	CTC ACA CTT CGC TGT TAG C
Cia1_Seq3_Rev	GCG TTA TAG TGA TAC AAA GG
Rpf1–For	CCT TCG TGT AAT ACA GGG TCG
Rpf1–Rev	GGG CGT GAA TGT AAG CGT GAC
Cfd1–For	AGT AAC TAC CCC ACA GAG TGT TGC
pRS_4xx_SacI	GGA TAA CAA TTT CAC ACA GG
T7_forward	TAA TAC GAC TCA CTA TAG G
T7_reverse	TGC TAG TTA TTG CTC AGC GG
Cyc–50_Rev	GGA CCT AGA CTT CAG GTT G
His_seq310	CTC ACA GAC GCG TTG AAT TG

Table S7. *Saccharomyces cerevisiae* strains.

Strain	Genotype	Background strain	Template	Ref.
W303-1A	MATa *leu2–3, 112 his3–11, 15 trp1–1, can1–100, ade2–1, ura 3–1*	–	–	(34)
Gal-*NFS1*	*W303*–1A *pNFS1*::*HIS3*–p*GAL1–10*	–	–	(35)
Gal-*NAR1*	*W303*–1A *pNAR1*::*HIS3*–p*GAL1–10*	–	–	(36)
Gal-*CIA2*	*W303*–1A *pCIA2*::*natNT2–GALL*	W303-1A	pYM_N27 (*Amp^R, natNT2)*	this work
Gal-*CIA1*	*W303*–1A *pCIA1*::*HIS3*–p*GAL1–10*	–	–	(37)
Gal-*CFD1*	*W303*–1A *pCFD1*::*HIS3*–*pGAL1–10*	–	_	(37)
Gal-*MAK16*	*W303*–1A *pMAK16*::*natNT2–GALL*	W303-1A	pYM_N27 (*Amp^R, natNT2)*	this work
Gal-*MAK16*/Gal-*NBP35*	*W303*–1A *pMAK16*::*natNT2–GALL*, *pNBP35*::*HIS3*–*pGAL1–10*	Gal-*MAK16*	pFA6a–HisMX6-Gal1-10 (*Amp^R, HIS3MX6)*	this work
Gal-*MAK16*/Gal-*CIA1*	*W303*–1A *pMAK16*::*natNT2*–p*GALL*, *pCIA1*::*HIS3*–p*GAL1–10*	Gal-*CIA1*	pYM_N27 (*Amp^R, natNT2)*	this work
Gal-*MAK16*/Gal-*CFD1*	*W303*–1A *pMAK16*::*natNT2–pGALL*, *pCFD1*::*HIS3*–*pGAL1–10*	Gal-*CFD1*	pYM_N27 (*Amp^R, natNT2)*	this work
Gal-*MAK16*/Gal-*RPF1*	*W303*–1A *pMAK16*::*natNT2–pGALL*, *pRPF1*::*HIS3*–*pGAL1–10*	Gal-*MAK16*	pYM_N27 with *natNT2* replaced by *HisMX6* (*Amp^R, HIS3MX6)*	this work

Table S8. *Escherichia coli* strains.

Strain	Genotype
NEB® 5-alpha (DH5α)	*fhuA2Δ(argF–lacZ)U169 phoA glnV44 Φ80Δ(lacZ)M15 gyrA96 recA1 relA1*
NEB® 10-beta	*Δ(ara–leu)7697 araD139 fhuA ΔlacX74 galK16 galE15 e14–ϕ80dlacZΔM15 recA1 endA1 nupG rpsL (StrR) rph spoT1 Δ(mrr–hsdRMS–mcrBC)*
NEB® 5-alpha F'I^q	F´ *proA*$^+$*B*$^+$ *lacI*^{q} Δ*(lacZ)M15 zzf*::*Tn10* (Tet^R) */ fhuA2*Δ*(argF–lacZ)U169 phoA glnV44 Φ80Δ(lacZ)M15 gyrA96 recA1 relA1*
T7 Express *lysY/I*^{q}	MiniF *lysY lacI*^{q}(Cam^R) */ fhuA2 lacZ*::*T7 gene1 [lon] ompT gal sulA11 R(mcr–73*::*miniTn10*–Tet^S*)2 [dcm] R(zgb–210*::*Tn10*–Tet^S*) endA1 Δ(mcrC–mrr) 114*::*IS10*

Table S9. Cloning primers.

Constructed plasmid	Primers	Sequence (5‘ → 3‘)	Starting plasmid, template
416-NP*MAK16* (*MAK16* nat. promoter yeast)	NP*MAK16*_SacI_For	GTA **GAG CTC** TTA GAA GAT AAA GTA GTG AAT TAC	SacI/XbaI cut 416-MET25, yeast genomic DNA
	NP*MAK16*_XbaI_Rev	GTA **TCT AGA** ATC CTC GTT GTA TTC TAA CCG TTG	
416-NP-Mak16 (yeast)	NP*MAK16*_SacI_For	GTA **GAG CTC** TTA GAA GAT AAA GTA GTG AAT TAC	SacI/XhoI cut 416-MET25, yeast genomic DNA
	Mak16_XhoI_Rev	ATG GTA **CTC GAG** TTA TTG TGC CAC TTC TTG CTC	
416-*MET25*-HA-Mak16 (yeast)	Mak16_XbaI_For	ATG GTA **TCT AGA** ATG TCC GAC GAA ATT GTT TGG	SpeI/XhoI cut 416-MET25-HA-Pol3CTD (38), yeast genomic DNA
	Mak16_XhoI_Rev	ATG GTA **CTC GAG** TTA TTG TGC CAC TTC TTG CTC	
416-NP-Mak16 (*E. cuniculi*)	Mak16Ecun_BamHI	TGG TA**G GAT CC**G ATG TCT GAC GAG AGC TTG TGG	BamHI/SalI cut 416-NP$_{MAK16}$, *E. cuniculi* genomic DNA
	Mak16Ecun_SalI	GGT A**GT CGA C**TC ACC ACT TCA TTG CTA CCT TCT	
416-NP-Mak16 (*H. sapiens*)	Mak16Hsap_BamHI	TGG TA**G GAT CC**C ATG CAG TCG GAT GAT GTT ATC	BamHI/SalI cut 416-NP$_{MAK16}$, human cDNA (clone MGC:57551)
	Mak16Hsap_SalI	TGG TA**G TCG AC**T CAC GTG GTT TTG GCT TTG GCC	
416-NP-Mak16 (*T. brucei*)	Mak16Tbru_BamHI	TGG TA**G GAT CC**G ATG AAC CAT GAT GAT GCG ATG	BamHI/SalI cut 416-NP$_{MAK16}$, *T. brucei* genomic DNA
	Mak16Tbru_SalI	GGT A**GT CGA C**TC ACC AAT CCA AAT CAG CCG TGC	
416-*MET25*-HA-Mak16 (*E. cuniculi*)	Mak16Ecun_SpeI	GGTA**ACTAGT**ATGTCTGACGAGA GCTTGTGGAG	SpeI/SalI cut 416-MET25-HA-Rev3CTD (38), 416-NP-Mak16 *(E. cuniculi)*
	Mak16Ecun_SalI	GGTA**GTCGAC**TCACCACTTCATT GCTACCTTCT	
416-*MET25*-HA-Mak16 (*H. sapiens*)	pRSxxx-SacI	GGA TAA CAA TTT CAC ACA GG (64 bp at the 5’ of SacI in 416)	SacI/SpeI cut 416-NP-Mak16 (*H. sapiens*), 416-MET25-HA-Pol3CTD (38)
	3HA_SpeI_rev	GGT A**AC TAG T**TC TCT AGT ATT CTC TGT CGG ACC	
416-*MET25*-HA-Mak16 (*T. brucei*)	pRSxxx-SacI	GGA TAA CAA TTT CAC ACA GG (64 bp at the 5’ of SacI in 416)	SacI/SpeI cut 416-NP-Mak16 (*T. brucei*), 416-MET25-HA-Pol3CTD (38)
	3HA_SpeI_rev	GGT A**AC TAG T**TC TCT AGT ATT CTC TGT CGG ACC	
pETDuet-1-His$_6$Mak16 (*H. sapiens*)	Mak16_BamHI_Hsfor	GCA CTG **GGA TCC** CAT GCA GTC GGA TGA TGT TAT CTG G	BamHI/SalI cut MCS1 of pETDuet-1, 416-NP-Mak16 (*H. sapiens*)
	Mak16_SalI_Hsrev	GGT A**GT CGA C**TC ACG TGG TTT TGG CTT TGG CCA CGG	
pETDuet-1-His$_6$Mak16 (yeast)	Mak16_BamHI_For	TGG TA**G GAT CC**T ATG TCC GAC GAA ATT GTT TGG	BamHI/SalI cut MCS1 of pETDuet-1, yeast genomic DNA
	Mak16_SalI_Rev	GGT A**GT CGA C**TT ATT GTG CCA CTT CTT GCT CAG	

pETDuet-1-Rpf1 (MCS2)	**NdeI_Rpf1_Sc_For(2)**	**GCA CTG** CAT ATG **GCT CTC GGT AAT GAG ATA AAC ATC**	**NdeI/XhoI cut MCS2 of pETDuet-1, yeast genomic DNA**
	XhoI_Rpf1_Rev	GCA CTG **CTC GAG** GTT TAC GAA TGG AAC ATA AAT AAA AC	
pETDuet-1-His$_6$Mak16/Rpf1	Mak16_BamHI_For	GCA CTG **GGA TCC** GAT GTC CGA CGA AAT TGT TTG GCA AGT G	BamHI/PstI cut MCS1 of pETDuet-1-Rpf1 (MCS2), yeast genomic DNA
	Mak16_PstI_Rev	GCA CTG **CTG CAG** TTA TTG TGC CAC TTC TTG CTC AGC	
pETDuet-1-His$_6$Mak16/Rpf1-Δ58	NdeI_Rpf1_Q58M_For	GCA CTG **CAT ATG** ACG ATA GAG AAC ACT AGA GTG TAC G	NdeI/XhoI cut pETDuet-1-His$_6$Mak16/Rpf1, yeast genomic DNA
	XhoI_Rpf1_Rev	GCA CTG **CTC GAG** GTT TAC GAA TGG AAC ATA AAT AAA AC	
414-NP-Cia1	Cia1_NP_SacI_For	ATG GTA **GAG CTC** CCG CCT GCT TAT TCG ACA TC	SacI/SalI cut 414-MET25, yeast genomic DNA
	Cia1_NP_SalI_Rev	ATG GTA **GTC GAC** CTA CGC TGC TTT TTC TAG AGA C	
414-*MET25*-Myc-Rpf1	Rpf1_SpeI_For	GCT CGT **ACT AGT** ATG GCT CTC GGT AAT GAG ATA AAC	SpeI/EcoRI cut 414-MET25-Myc-Cfd1 (27), yeast genomic DNA
	Rpf1_EcoRI_Rev	GCT CGT **GAA TTC** CGA ATG GAA CAC TAT AAA TAA AAC	

Table S10. Mutagenesis primers.

Constructed plasmid	Primers	Sequence (5' → 3')	Mutagenized plasmid
416-NP-Mak16 (yeast) C15A	Mak16_C15A_for	TCAAAGCTTCGCCTCTCATAGAATTAAGGCACC	416-NP-Mak16 wildtype (yeast)
	Mak16_C15A_rev	CTATGAGAGGCGAAGCTTTGATTAATCACTTGC	
416-NP-Mak16 (yeast) C28A	Mak16_C28A_for	GTCAAAATTTTGCCAGAAATGAGTATAACGTCA	416-NP-Mak16 wildtype (yeast)
	Mak16_C28A_rev	TCATTTCTGGCAAAATTTTGACCATTAGGTGCC	
416-NP-Mak16 (yeast) C38A	Mak16_C38A_for	CGTCACTGGGCTAGCTACAAGGCAATCATGCCC	416-NP-Mak16 wildtype (yeast)
	Mak16_C38A_rev	TTGTAGCTAGCCCAGTGACGTTATACTCATTTC	
416-NP-Mak16 (yeast) C15A/C38A	Mak16_C38A_for	CGTCACTGGGCTAGCTACAAGGCAATCATGCCC	416-NP-Mak16 C15A (yeast)
	Mak16_C38A_rev	TTGTAGCTAGCCCAGTGACGTTATACTCATTTC	
416-NP-Mak16 (yeast) C43A	Mak16_C43A_for	ATCAGCCCCGCTAGCCAACTCCAAGTATGCAAC	416-NP-Mak16 wildtype (yeast)
	Mak16_C43A_rev	TTGGCTAGCGGGGCTGATTGCCTTGTACACAAC	
416-NP-Mak16 (yeast) C55A	Mak16_C55A_for	ACAGTGAAGGCTGACAATGGGAAACTGTACTTG	416-NP-Mak16 wildtype (yeast)
	Mak16_C55A_rev	CCATTGTCAGCCTTCACTGTTGCATACTTGGAG	
416-NP-Mak16 (yeast) C108A	Mak16_C108A_for	CGTCATAAGGCTAAACAGAGATTTACAAAATTG	416-NP-Mak16 wildtype (yeast)
	Mak16_C108A_rev	TCTGTTTAGCCTTATGACGGAAAAACTTGCTCC	
416-*MET25*-HA-Mak16 (yeast) C15A	Mak16_C15A_for	TCAAAGCTTCGCCTCTCATAGAATTAAGGCACC	416-*MET25*-HA-Mak16 wildtype (yeast)
	Mak16_C15A_rev	CTATGAGAGGCGAAGCTTTGATTAATCACTTGC	
416-*MET25*-HA-Mak16 (yeast) C28A	Mak16_C28A_for	GTCAAAATTTTGCCAGAAATGAGTATAACGTCA	416-*MET25*-HA-Mak16 wildtype (yeast)
	Mak16_C28A_rev	TCATTTCTGGCAAAATTTTGACCATTAGGTGCC	
416-*MET25*-HA-Mak16 (yeast) C38A	Mak16_C38A_for	CGTCACTGGGCTAGCTACAAGGCAATCATGCCC	416-*MET25*-HA-Mak16 wildtype (yeast)
	Mak16_C38A_rev	TTGTAGCTAGCCCAGTGACGTTATACTCATTTC	
416-*MET25*-HA-Mak16 (yeast) C15A/C38A	Mak16_C38A_for	TCAAAGCTTCGCCTCTCATAGAATTAAGGCACC	416-*MET25*-HA-Mak16 C15A (yeast)
	Mak16_C38A_rev	CTATGAGAGGCGAAGCTTTGATTAATCACTTGC	
416-*MET25*-HA-Mak16 (yeast) C55A	Mak16_C55A_for	ACAGTGAAGGCTGACAATGGGAAACTGTACTTG	416-*MET25*-HA-Mak16 wildtype (yeast)
	Mak16_C55A_rev	CCATTGTCAGCCTTCACTGTTGCATACTTGGAG	

Table S11. Plasmids for yeast.

Plasmid	Promoter	Source gene	Use	Ref.
416-*MET25*	*MET25*	–	^{55}Fe incorporation, IP RNA isolation	(4)
414-MET25	*MET25*	–	Cloning, as control, IP	(4)
416-NP (yeast *MAK16* promotor, NP)	*MAK16*	*S. cerevisiae*	Cloning, RNA isolation growth complementation	this work
416-NP-Mak16	*MAK16*	*S. cerevisiae*	RNA isolation growth complementation	this work
416-NP-Mak16$_{E.cun}$	*MAK16*	*E. cuniculi*	growth complementation	this work
416-NP-Mak16$_{H.sap}$	*MAK16*	*H. sapiens*	growth complementation	this work
416-NP-Mak16$_{T. bru}$	*MAK16*	*T. brucei*	growth complementation	this work
416-*MET25*-HA-Mak16	*MET25*	*S. cerevisiae*	^{55}Fe incorporation, growth complementation	this work
416-*MET25*-HA-Mak16$_{E.cun}$	*MET25*	*E. cuniculi*	^{55}Fe incorporation, growth complementation	this work
416-*MET25*-HA-Mak16$_{H.sap}$	*MET25*	*H. sapiens*	^{55}Fe incorporation, growth complementation	this work
416-*MET25*-HA-Mak16$_{T.bru}$	*MET25*	*T. brucei*	^{55}Fe incorporation, growth complementation	this work
416-NP-Mak16-C15A	*MAK16*	*S. cerevisiae*	RNA isolation growth complementation	this work
416-NP-Mak16-C28A	*MAK16*	*S. cerevisiae*	RNA isolation growth complementation	this work
416-NP-Mak16-C38A	*MAK16*	*S. cerevisiae*	RNA isolation growth complementation	this work
416-NP-Mak16-C15A/C38A	*MAK16*	*S. cerevisiae*	RNA isolation growth complementation	this work
416-NP-Mak16-C43A	*MAK16*	*S. cerevisiae*	RNA isolation growth complementation	this work
416-NP-Mak16-C55A	*MAK16*	*S. cerevisiae*	growth complementation	this work
416-NP-Mak16-C108A	*MAK16*	*S. cerevisiae*	growth complementation	this work
414-NP-Cia1	*CIA1*	*S. cerevisiae*	growth complementation	this work
414-*MET25*-Myc-Cfd1	*MET25*	*S. cerevisiae*	growth complementation	(27)
414-*MET25*-Myc-Nbp35	*MET25*	*S. cerevisiae*	growth complementation	(27)
414-*MET25*-Myc-Rpf1	*RPF1*	*S. cerevisiae*	IP	this work
416-*MET25*-HA-Mak16-C28A	*MET25*	*S. cerevisiae*	IP	this work
416-*MET25*-HA-Mak16-C38A	*MET25*	*S. cerevisiae*	IP	this work
416-*MET25*-HA-Mak16-C15A/C38A	*MET25*	*S. cerevisiae*	IP	this work
416-*MET*25-HA-Mak16-C55A	*MET25*	*S. cerevisiae*	IP	this work

Table S12. Plasmids for expression in *Escherichia coli*.

Name	Features	Ref.
pETDuet-1-His_6Mak16_H. sap	MCSI: His_6-Mak16 human	this work
pETDuet-1-His_6Mak16/Rpf1 yeast	MCSI: His_6-Mak16 yeast MCSII: Rpf1 yeast full length	this work
pETDuet-1-His_6Mak16/Rpf1-Δ58 yeast	MCSI: His_6-Mak16 yeast MCSII: Rpf1-Δ58 yeast	this work

Table S13. Antibodies.

Antibodies	Type	Dilution	Source
Anti-HA (F-7) sc-7392	monoclonal	1:1000 or 1:2000	Santa Cruz Biotechnology
Anti-Myc (9E10) sc-40	monoclonal	1:2000	Santa Cruz Biotechnology
Anti-His (1-21315)	monoclonal	1:1000	Invitrogen
Anti-Nfs1	polyclonal	1:1000	Rabbit (Prof. Lill, Marburg)
Anti-Nar1	polyclonal	1:1000	Rabbit (Prof. Lill, Marburg)
Anti-Cia2	polyclonal	1:1000	Rabbit (Prof. Lill, Marburg)
Anti-Porin	polyclonal	1:2000	Rabbit (Prof. Lill, Marburg)
Goat anti-rabbit IgG-HRP	monoclonal	1:5000	Santa Cruz Biotechnology
Goat-anti mouse IgG-HRP	monoclonal	1:10000	Santa Cruz Biotechnology

SI References

1. C. Janke, *et al*., A versatile toolbox for PCR-based tagging of yeast genes: new fluorescent proteins, more markers and promoter substitution cassettes. *Yeast* **21**, 947–962 (2004).
2. R. D. Gietz, R. A. Woods, Transformation of yeast by lithium acetate/single-stranded carrier DNA/polyethylene glycol method. *Methods Enzymol.* **350**, 87–96 (2002).
3. U. Mühlenhoff, N. Richhardt, M. Ristow, G. Kispal, R. Lill, The yeast frataxin homolog Yfh1p plays a specific role in the maturation of cellular Fe/S proteins. *Hum. Mol. Genet.* **11**, 2025–2036 (2002).
4. D. Mumberg, R. Müller, M. Funk, Yeast vectors for the controlled expression of heterologous proteins in different genetic backgrounds. *Gene* **156**, 119–122 (1995).
5. L. Zheng, U. Baumann, J.-L. Reymond, An efficient one-step site-directed and site-saturation mutagenesis protocol. *Nucleic Acids Res.* **32**, e115 (2004).
6. J. A. Gibson, M. Marshall, The counting efficiency for ^{55}Fe and other E.C. nuclides in liquid scintillator solutions. *Int. J. Appl. Radiat. Isot.* **23**, 321–328 (1972).
7. A. J. Pierik, R. B. Wolbert, P. H. Mutsaers, W. R. Hagen, C. Veeger, Purification and biochemical characterization of a putative [6Fe-6S] prismane-cluster-containing protein from *Desulfovibrio vulgaris* (Hildenborough). *Eur. J. Biochem.* **206**, 697–704 (1992).
8. W. R. Hagen, Very Low-Frequency Broadband Electron Paramagnetic Resonance Spectroscopy of Metalloproteins. *J. Phys. Chem. A* **125**, 3208–3218 (2021).
9. V. Schünemann, “From Small Molecules to Complex Systems: A Survey of Chemical and Biological Applications of the Mössbauer Effect” in *Y. Yoshida, G. Langouche (Eds.) 2021 – Modern Mössbauer Spectroscopy*, pp. 173–219.
10. H. P. Gunnlaugsson, Spreadsheet based analysis of Mössbauer spectra. *Hyperfine Interact.* **237**, 79 (2016).
11. F. Corpet, Multiple sequence alignment with hierarchical clustering. *Nucleic Acids Res.* **16**, 10881–10890 (1988).
12. P. Middleton, D. P. Dickson, C. E. Johnson, J. D. Rush, Interpretation of the Mössbauer spectra of the four-iron ferredoxin from *Bacillus stearothermophilus*. *Eur. J. Biochem.* **88**, 135–141 (1978).
13. M. C. Evans, D. O. Hall, C. E. Johnson, Hyperfine structure of ^{57}Fe iron in the Mössbauer spectrum of the high-potential iron protein from *Chromatium*. *Biochem. J.* **119**, 289–291 (1970).
14. D. P. Dickson, *et al*., Mössbauer effect in the high-potential iron-sulphur protein from *Chromatium*. Evidence for the state of the iron atoms. *Biochem. J.* **139**, 105–108 (1974).
15. R. N. Mullinger, *et al*., Physicochemical characterization of the four-iron-four-sulphide ferredoxin from *Bacillus stearothermophilus*. *Biochem. J.* **151**, 75–83 (1975).
16. S. J. Vollmer, R. L. Switzer, P. G. Debrunner, Oxidation-reduction properties of the iron-sulfur cluster in *Bacillus subtilis* glutamine phosphoribosylpyrophosphate amidotransferase. *J. Biol. Chem.* **258**, 14284–14293 (1983).
17. P. A. Lindahl, E. P. Day, T. A. Kent, W. H. Orme-Johnson, E. Münck, Mössbauer, EPR, and magnetization studies of the *Azotobacter vinelandii* Fe protein. *J. Biol. Chem.* **260**, 11160–11173 (1985).
18. V. Petrouleas, J. J. Brand, K. G. Parrett, J. H. Golbeck, A Mössbauer analysis of the low-potential iron-sulfur center in photosystem I: spectroscopic evidence that F_X is a 4Fe-4S cluster. *Biochemistry* **28**, 8980–8983 (1989).
19. J. Lampreia, *et al*., The active centers of adenylylsulfate reductase from *Desulfovibrio gigas*. Characterization and spectroscopic studies. *Eur. J. Biochem.* **188**, 653–664 (1990).
20. J. Caldeira, *et al*., EPR and Mössbauer spectroscopic studies on enoate reductase. *J. Biol. Chem.* **271**, 18743–18748 (1996).
21. D. F. Becker, U. Leartsakulpanich, K. K. Surerus, J. G. Ferry, S. W. Ragsdale, Electrochemical and spectroscopic properties of the iron-sulfur flavoprotein from *Methanosarcina thermophila*. *J. Biol. Chem.* **273**, 26462–26469 (1998).

22. M. Blokesch, *et al*., The complex between hydrogenase-maturation proteins HypC and HypD is an intermediate in the supply of cyanide to the active site iron of NiFe-hydrogenases. *J. Mol. Biol.* **344**, 155–167 (2004).

23. M. L. Antonkine, *et al.*, Chemical rescue of a site-modified ligand to a [4Fe-4S] cluster in PsaC, a bacterial-like dicluster ferredoxin bound to Photosystem I. *Biochim. Biophys. Acta* **1767**, 712–724 (2007).

24. D. Barthelme, *et al.*, Structural organization of essential iron-sulfur clusters in the evolutionarily highly conserved ATP-binding cassette protein ABCE1. *J. Biol. Chem.* **282**, 14598–14607 (2007).

25. M. Müllner, *et al*., A PAS domain with an oxygen labile $[4Fe\text{-}4S]^{2+}$ cluster in the oxygen sensor kinase NreB of *Staphylococcus carnosus*. *Biochemistry* **47**, 13921–13932 (2008).

26. L. J. Rather, E. Bill, W. Ismail, G. Fuchs, The reducing component BoxA of benzoyl-coenzyme A epoxidase from *Azoarcus evansii* is a [4Fe-4S] protein. *Biochim. Biophys. Acta* **1814**, 1609–1615 (2011).

27. D. J. Netz, *et al*., A bridging [4Fe-4S] cluster and nucleotide binding are essential for function of the Cfd1-Nbp35 complex as a scaffold in iron-sulfur protein maturation. *J. Biol. Chem.* **287**, 12365–12378 (2012).

28. M. Hilberg, *et al*., Identification of FeS clusters in the glycyl-radical enzyme benzylsuccinate synthase via EPR and Mössbauer spectroscopy. *J. Biol. Inorg. Chem.* **17**, 49–56 (2012).

29. T. O. Bauer, D. Graf, T. Lamparter, V. Schünemann, Characterization of the photolyase-like iron sulfur protein PhrB from *Agrobacterium tumefaciens* by Mössbauer spectroscopy. *Hyperfine Interact.* **226**, 445–449 (2014).

30. D. J. Netz, *et al*., The conserved protein Dre2 uses essential [2Fe-2S] and [4Fe-4S] clusters for its function in cytosolic iron-sulfur protein assembly. *Biochem. J.* **473**, 2073–2085 (2016).

31. J. J. Moura, *et al*., Interconversions of [3Fe-3S] and [4Fe-4S] clusters. Mössbauer and electron paramagnetic resonance studies of *Desulfovibrio gigas* ferredoxin II. *J. Biol. Chem.* **257**, 6259–6267 (1982).

32. C. L. Thompson, *et al*., Mössbauer effect in the eight-iron ferredoxin from *Clostridium pasteurianum*. Evidence for the state of the iron atoms. *Biochem. J.* **139**, 97–103 (1974).

33. M. Hans, W. Buckel, E. Bill, The iron-sulfur clusters in 2-hydroxyglutaryl-CoA dehydratase from *Acidaminococcus fermentans*. Biochemical and spectroscopic investigations. *Eur. J. Biochem.* **267**, 7082–7093 (2000).

34. B. J. Thomas, R. Rothstein, Elevated recombination rates in transcriptionally active DNA. *Cell* **56**, 619–630 (1989).

35. U. Mühlenhoff, *et al*., Functional characterization of the eukaryotic cysteine desulfurase Nfs1p from *Saccharomyces cerevisiae*. *J. Biol. Chem.* **279**, 36906–36915 (2004).

36. J. Balk, A. J. Pierik, D. J. A. Netz, U. Mühlenhoff, R. Lill, The hydrogenase-like Nar1p is essential for maturation of cytosolic and nuclear iron–sulphur proteins. *EMBO J.* **23**, 2105–2115 (2004).

37. J. Balk, D. J. Netz, M. Stümpfig, U. Mühlenhoff, R. Lill, The essential WD40 protein Cia1 is involved in a late step of cytosolic and nuclear iron-sulfur protein assembly. *Mol. Cell. Biol.* **25**, 10833–10841 (2005).

38. D. J. Netz, *et al*., Eukaryotic DNA polymerases require an iron-sulfur cluster for the formation of active complexes. *Nat. Chem. Biol.* **8**, 125–132 (2011).